



Michigan Technological University
Create the Future Digital Commons @ Michigan Tech

Dissertations, Master's Theses and Master's
Reports - Open

Dissertations, Master's Theses and Master's
Reports

2013

Dysprosium transport in Nd-Fe-B pellets

Parawee Pumwongpitak
Michigan Technological University

Follow this and additional works at: <https://digitalcommons.mtu.edu/etds>


 Part of the [Materials Science and Engineering Commons](#)

Copyright 2013 Parawee Pumwongpitak

Recommended Citation

Pumwongpitak, Parawee, "Dysprosium transport in Nd-Fe-B pellets", Master's Thesis, Michigan Technological University, 2013.
<https://doi.org/10.37099/mtu.dc.etds/616>

Follow this and additional works at: <https://digitalcommons.mtu.edu/etds>

 Part of the [Materials Science and Engineering Commons](#)

DYSPROSIUM TRANSPORT IN Nd-Fe-B PELLETS

By

Parawee Pumwongpitak

A THESIS

Submitted in partial fulfillment of the requirements for the degree of

MASTER OF SCIENCE

In Materials Science and Engineering

MICHIGAN TECHNOLOGICAL UNIVERSITY

2013

© 2013 Parawee Pumwongpitak

This thesis has been approved in partial fulfillment of the requirements for the Degree of
MASTER OF SCIENCE in Materials Science and Engineering

Department of Materials Science and Engineering

Thesis Advisor: Dr. Stephen A. Hackney

Committee Member: Dr. Peter D. Moran

Committee Member: Dr. Yongmei M. Jin

Committee Member: Dr. John A. Jaszczak

Department Chair: Dr. Stephen L. Kampe

Table of Contents

List of Figures	v
List of Tables	vii
Acknowledgements	viii
Abstract	ix
Chapter 1	1
Introduction and Background	1
1.1 Background	5
Chapter 2	11
Experimental Procedure	11
2.1 Diffusion of Dy in $\text{Nd}_2\text{Fe}_{14}\text{B}$ composition	11
2.2 Dy Transport Control during the Sintering Process	13
2.2.1 Preparation of layered pellets	13
2.2.2 Characterization of the layered-pellets	16
2.3 The Eutectic liquid and the solid reaction study	18
2.3.1 Dy-Coated ribbons preparation	18
2.3.2 Characterization of Dy-Coated ribbons	18
Chapter 3	19
Results and discussions	19
3.1 Dy Transport Control during the Sintering Process	21
3.1.1 Increasing the melting point and spacing of the Dy source	21
3.1.2 High melting point Dy source	23
3.1.3 Schematic of transient liquid sintering	24
3.1.4 Layer pellet microstructure	26
3.2 The Eutectic liquid and the solid reaction study	36
3.2.1 Diffusion of Dy in $\text{Nd}_{2.7}\text{Fe}_{14}\text{B}_{1.4}$ composition (Nd rich liquid diffuses into $\text{Dy}_2\text{Fe}_{14}\text{B}$ grain)	36
3.2.2 $\text{Nd}_{2.7}\text{Fe}_{14}\text{B}_{1.4}$ ribbons morphology	39
3.2.3 $\text{Dy}_{2.34}\text{Fe}$ coated $\text{Nd}_{2.7}\text{Fe}_{14}\text{B}_{1.4}$ ribbons before heat treatment	40
3.2.4 The results of reaction between Nd ribbons and Dy:Fe coating	42
3.3 The comparison of the effective diffusion length	61

Conclusions.....	64
References.....	66
Appendix A: The composition of eutectic and solid phases in $\text{Nd}_2\text{Fe}_{14}\text{B}$ layer away from the center layer of the $\text{Nd}_{2.7}\text{Fe}_{14}\text{B}_{1.4}/30\%\text{Dy}_{2.34}\text{Fe}/\text{Nd}_{2.7}\text{Fe}_{14}\text{B}_{1.4}$ pellet.....	69
Appendix B: The composition of eutectic and solid phases in $\text{Nd}_2\text{Fe}_{14}\text{B}$ layer away from the center layer of the $\text{Nd}_{2.7}\text{Fe}_{14}\text{B}_{1.4}/30\%\text{Dy}_{2.34}\text{Fe}$ plus 1.5 mole Fe_{14}B per mole of Nd liquid mixing powder/ $\text{Nd}_{2.7}\text{Fe}_{14}\text{B}_{1.4}$ pellet.....	71
Appendix C: The composition of eutectic and solid phases in $\text{Nd}_2\text{Fe}_{14}\text{B}$ layer away from the center layer of the $\text{Nd}_{2.7}\text{Fe}_{14}\text{B}_{1.4}/\text{Dy}_2\text{Fe}_{14}\text{B}$ plus 2at% B/ $\text{Nd}_{2.7}\text{Fe}_{14}\text{B}_{1.4}$ pellet.....	73
Appendix D: This letter is for Figure 1.1 and 3.4.....	75
Appendix E: This letter is for Figure 3.2	76
Appendix F: This letter is for Figure 3.3	77

List of Figures

Figure 1.1 (a) Ternary isotherm of Nd-Fe-B phase diagrams [5]. (b) Heterogeneous nucleation of magnetic domain in a reversing field	2
Figure 1.2 Proposal for lean rare earth, high coercivity, high temperature Nd-Fe-B based magnets using grain surface enrichment with heavy rare earth.	3
Figure 1.3 The illustration of the core-shell structure of Dy covered Nd ₂ Fe ₁₄ B grains.	4
Figure 1.4 (a) Back scattered image showing rare earth rich phases (bright) associated with the eutectic liquid solidification. (b-d) EDS Element maps for Nd, Dy and O. (Figure adapted by author from [28])	6
Figure 1.5 Diffusion coefficients for volume diffusion, grain boundary diffusion, liquid phase diffusion, and diffusion of Dy at 1050°C	8
Figure 1.6 (a) Dissolution:reprecipitation driven by Gibbs-Thompson Effect (b) dissolution:reprecipitation driven by free energy of mixing.	10
Figure 2.1 The illustration of three layered pellets.	16
Figure 2.2 The illustration shows the points were collected from the layered pellet.	17
Figure 2.3 Schematic representation of Physical Vapor Deposition process.	18
Figure 3.1 (a) The Nd-Fe-B ternary phase diagram [5] , (b) Nd-Fe-B sintered two phase structure with RE rich eutectic phase seen as the ductile phase at the grain boundary in the fracture surface cross section. (c) Nd-Fe-B sintered two phases structure with RE rich eutectic phase shown as bright in the BSE polished surface.	20
Figure 3.2 Dy-Fe binary phase diagram [34].....	22
Figure 3.3 Dy-Fe-B phase diagram [35]	23
Figure 3.4 The ternary Nd-Fe-B phase diagram [5]	25
Figure 3.5 The schematic shows Fe ₁₄ B and Nd rich liquid mechanism.....	25
Figure 3.6 SEM images in SEI mode at low magnification of Nd _{2.7} Fe ₁₄ B _{1.4} /30%Dy _{2.34} Fe/Nd _{2.7} Fe ₁₄ B _{1.4} pellet (a), Nd _{2.7} Fe ₁₄ B _{1.4} /30% Dy _{2.34} Fe plus 1.5 mole Fe ₁₄ B per mole of Nd liquid mixing powder/Nd _{2.7} Fe ₁₄ B _{1.4} pellet (b), and Nd _{2.7} Fe ₁₄ B _{1.4} /Dy ₂ Fe ₁₄ B plus 2at%B/ Nd _{2.7} Fe ₁₄ B _{1.4} pellet (c).....	27
Figure 3.7 SEM image in BSE mode of 30%Dy _{2.34} Fe center layer.....	28
Figure 3.8 SEM images in BSE mode of Nd _{2.7} Fe ₁₄ B _{1.4} layer in Nd _{2.7} Fe ₁₄ B _{1.4} /30%Dy _{2.34} Fe/Nd _{2.7} Fe ₁₄ B _{1.4} pellet. At position away from interface 100 μm (a), 350 μm (b), and 550 μm (c).	29
Figure 3.9 The concentration of Dy in eutectic and gray phases of Nd _{2.7} Fe ₁₄ B _{1.4} /30%Dy _{2.34} Fe/Nd _{2.7} Fe ₁₄ B _{1.4} pellet at each distance from the center layer.....	30
Figure 3.10 SEM image in BSE mode of 30% Dy _{2.34} Fe plus 1.5 Mole Fe ₁₄ B per mole of Nd liquid center layer	31
Figure 3.11 SEM images in BSE mode of Nd ₂ Fe ₁₄ B layer in Nd _{2.7} Fe ₁₄ B _{1.4} /30% Dy _{2.34} Fe plus 1.5 Mole Fe ₁₄ B per mole of Nd liquid mixing powder / Nd _{2.7} Fe ₁₄ B _{1.4} pellet. At position away from interface 100 μm (a), 350 μm (b), 550 μm (c), and 850 μm (d).	32

Figure 3.12	The concentration of Dy in eutectic and gray phases of $\text{Nd}_{2.7}\text{Fe}_{14}\text{B}_{1.4}/30\%$ $\text{Dy}_{2.34}\text{Fe}$ plus 1.5 Mole Fe_{14}B per mole of Nd liquid mixing powder/ $\text{Nd}_{2.7}\text{Fe}_{14}\text{B}_{1.4}$ pellet at each distance from the center layer	33
Figure 3.13	Backscattered image of $\text{Dy}_2\text{Fe}_{14}\text{B}$ plus 2at% B at the center layer	34
Figure 3.14	SEM images in BSE mode of $\text{Nd}_2\text{Fe}_{14}\text{B}$ layer in $\text{Nd}_{2.7}\text{Fe}_{14}\text{B}_{1.4}/\text{Dy}_2\text{Fe}_{14}\text{B}$ plus 2at% B/ $\text{Nd}_{2.7}\text{Fe}_{14}\text{B}_{1.4}$ pellet. At position away from interface 100 μm (a), 350 μm (b), 550 μm (c), and 850 μm (d).	35
Figure 3.15	The concentration of Dy in eutectic and gray phases of $\text{Nd}_{2.7}\text{Fe}_{14}\text{B}_{1.4}/\text{Dy}_2\text{Fe}_{14}\text{B}$ plus 2at% B/ $\text{Nd}_{2.7}\text{Fe}_{14}\text{B}_{1.4}$ pellet at each distance from the center layer	35
Figure 3.16	BSE image of Nd rich liquid penetrating into Dy ribbon.....	36
Figure 3.17	The standardless EDS results of Dy ribbon that attacked by Nd eutectic liquid. (a) area 1 (b) area 2 (c) area 3	38
Figure 3.18	The cross section micrograph of $\text{Nd}_{2.7}\text{Fe}_{14}\text{B}_{1.4}$ melt spun ribbons.	40
Figure 3.19	FE-SEM image of $\text{Dy}_{2.34}\text{Fe}$ coated $\text{Nd}_{2.7}\text{Fe}_{14}\text{B}_{1.4}$ ribbons before heat treatment.....	41
Figure 3.20	EDS spectrum of $\text{Dy}_{2.34}\text{Fe}$ coated $\text{Nd}_{2.7}\text{Fe}_{14}\text{B}_{1.4}$ ribbons before heat treatment	42
Figure 3.21	(a,b) FE-SEM images the cross section of thermal treated ribbon at 850°C (c) EDS spectrum from the reaction area A in figure (b).....	43
Figure 3.22	FE-SEM image of the cross section of the thermal treated ribbon at 850°C for 1 hour.....	44
Figure 3.23	(a,b) FE-SEM images the cross section of thermal treated ribbon at 950°C.	45
Figure 3.24	(a,b) FE-SEM images the cross section of thermal treated ribbon at 950°C.	46
Figure 3.25	FE-SEM image of the cross section of thermal treated ribbon at 950°C	46
Figure 3.26	The schematic illustrates mechanism during thermal treatment process.	47
Figure 3.27	FE-SEM images of the fracture surface of thermal treated ribbon at (a) 850°C and (b) 950°C. (c) Sintered $\text{Nd}_{2.7}\text{Fe}_{14}\text{B}_{1.4}$ fracture surface showing ductile Nd rich phase at the grain boundary.....	50
Figure 3.28	Illustration of the proposed solution/precipitation process	53
Figure 3.29	Concentration profile of Dy vary with depth from the interface for $\text{Dy}_{2.34}\text{Fe}$ as Dy source (a) Dy concentration in eutectic phase (b) Dy concentration in the grain	57
Figure 3.30	Concentration profile of Dy vary with depth from the interface for $\text{Dy}_{2.34}\text{Fe}$ plus Fe_{14}B as Dy source (a) Dy concentration in eutectic phase (b) Dy concentration in the grain	58
Figure 3.31	Concentration profile of Dy vary with depth from the interface for $\text{Dy}_2\text{Fe}_{14}\text{B}$ plus 2at%B as Dy source (a) Dy concentration in eutectic phase (b) Dy concentration in the grain	59

List of Tables

Table 2.1 Chemical composition of $\text{Nd}_{2.7}\text{Fe}_{14}\text{B}_{1.4}$ alloy powder	14
Table 3.1 Diffusion coefficient and effective diffusion length of $\text{Dy}_{2.34}\text{Fe}$ coated $\text{Nd}_{2.4}\text{Fe}_{14}\text{B}_{1.4}$ ribbon.....	48
Table 3.2 The diffusion coefficient, velocity, and reaction between liquid and solid parameters.....	60
Table 3.3 Porosity and tortuosity factors in catalyst materials [41]	61
Table 3.4 The diffusion coefficient and effective diffusion length of layered pellets and coated $\text{Nd}_{2.4}\text{Fe}_{14}\text{B}_{1.4}$ ribbons.....	63

Acknowledgements

I am grateful to all of the friends and acquaintances that have helped me along this thesis. First, I would like to express my deepest appreciation to Prof. Stephen A. Hackney for his guidance and time to review my thesis. I would like to thank Dr. Edward P. Becker, Dr. Yucong Wang at General Motors Company for their support. I would like to give thanks to Dr. Peter D. Moran, Dr. Yongmei M. Jin and Dr. John A. Jaszczak for reviewing my work and serving on my committee.

My special thanks are also extended to Paul Fraley, Owen P. Mills, Ruth I. Kramer, Li Chen, and Jie Li for helping me when I needed help.

I would to express my acknowledge to Royal Thai Government and Thailand Institute of Scientific and Technology Research (TISTR) who provided scholarship support for my study in US.

Finally, I would like to thank my family and friends for their love and support.

Abstract

The addition of heavy rare earth (RE) elements to $\text{Nd}_2\text{Fe}_{14}\text{B}$ based magnets to form $(\text{Nd,Dy})_2\text{Fe}_{14}\text{B}$ is known to increase the coercivity and high temperature performance required for hybrid vehicle electric motors and other extreme temperature applications. Attempts to conserve heavy rare earth elements for high temperature $(\text{RE})_2\text{Fe}_{14}\text{B}$ based magnets have led to the development of a grain boundary diffusion process for bulk magnets. This process relies on transport of a heavy rare earth, such as Dy, into a bulk $\text{Nd}_2\text{Fe}_{14}\text{B}$ magnet along pores, a low volume fraction of eutectic liquid along grain boundary grain triple junctions and grain boundaries. This enriches the grain surfaces in Dy through the thickness of the bulk magnet, leading to larger increases in coercivity with a smaller Dy concentration than can be achieved with homogeneous alloys. Attempts to carry out the same process during sintering require significant control of Dy transport efficiency.

The macroscopic transport of Dy in $\text{Nd}_{2.7}\text{Fe}_{14}\text{B}_{1.4}$ based powder packs is studied using a 'layered' pellet, where $\text{Nd}_{2.7}\text{Fe}_{14}\text{B}_{1.4}$ powder is an interlayer and Dy source as a center layer. The sintering of this layered pellet provided evidence for very large effective diffusion lengths aided by Dy rich liquid flow through connected porosity. Approaches to

controlling Dy transportation include decreasing the liquid phase transport capability of the powder pack by increasing the melting point of the Dy source and the decreasing amount of RE rich liquid in the powder packs.

The solid-liquid reaction is studied in which melt spun $\text{Nd}_{2.7}\text{Fe}_{14}\text{B}_{1.4}$ ribbons are PVD coated with Dy-Fe eutectic composition and then thermally treated. The resulting microstructure from the reaction between Dy-Fe eutectic coating and $\text{Nd}_{2.7}\text{Fe}_{14}\text{B}_{1.4}$ ribbon is interpreted as support for a proposed dissolution/precipitation process between solid and liquid phases.

The estimate the diffusion coefficient and the effective diffusion length of Dy sources in $\text{Nd}_{2.7}\text{Fe}_{14}\text{B}_{1.4}$ layered pellets and melt spun ribbons were obtained from the calculation of Fick's second law combined with EDS results from the experiment. The results indicate that the effective diffusion coefficient of Dy in the layered pellets is higher than the diffusion in ribbons due to its higher porosity than ribbons.

Chapter 1

Introduction and Background

Sintered Nd-Fe-B magnetic materials are essential components in electric motors for hybrid electric vehicles (HEVs) and electric vehicles (EVs) because of their high maximum energy product $(BH)_{\max}$ and high coercivity as compared to other magnets [1-3]. The conventional sintered magnet is actually produced by liquid phase sintered through accessing the low temperature eutectic (Figure 1.1(a)). Different manufacturers use slightly different compositions. Boron rich stoichiometries, such as $\text{Nd}_{2.7}\text{Fe}_{14}\text{B}_{1.4}$, will have three main phases present at room temperature equilibrium, $\text{Nd}_2\text{Fe}_{14}\text{B}$, Nd-rich solid solution, and B-rich ($\text{Nd}_{1+d}\text{Fe}_4\text{B}_4$) phases. Boron poor stoichiometries such as $\text{Nd}_{2.7}\text{Fe}_{14}\text{B}_{0.95}$ will only show the $\text{Nd}_2\text{Fe}_{14}\text{B}$ and Nd-rich solid solution at equilibrium below the eutectic temperature. The Nd-rich solid solution phase precipitates from the eutectic liquid below 665°C and presents along the grain boundaries. This is thought to reduce grain boundary defects, which act as magnetic domain nucleation sites [1, 4]. Magnetic domain nucleation at grain boundaries is a major contributing factor to demagnetization in reverse fields, and can destroy the functionality of a magnet operating in an electric motor (Figure 1.1 (b)).

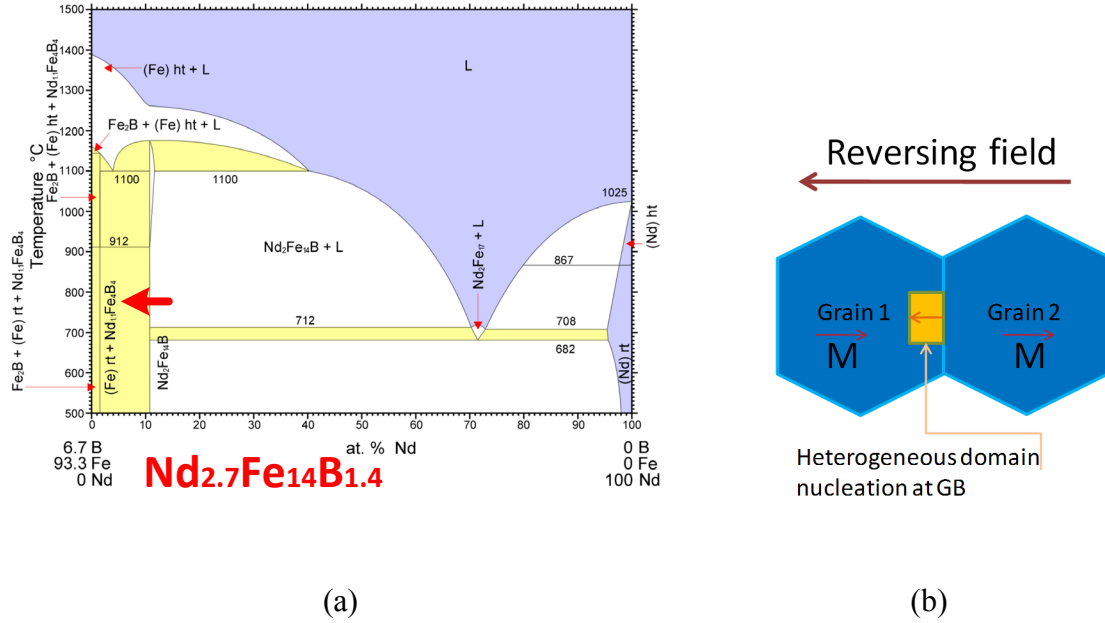


Figure 1.1 (a) Ternary isotherm of Nd-Fe-B phase diagrams [5]. (b) Heterogeneous nucleation of magnetic domain in a reversing field

The coercivity (H_c) of NdFeB magnets will drop drastically above 100°C (2) due to the low Curie temperature (313°C) [6-8], leading to a reduction of the saturation magnetization with increasing the temperature. Elevated temperature destruction of magnetic performance is also exacerbated by surface defects such as cracks, oxide particles, triple junctions and grain boundaries that have low anisotropy and act as nucleation site of reversed magnetic domains [8, 9].

Dy₂Fe₁₄B and Tb₂Fe₁₄B have higher Curie temperature and higher anisotropy constants than Nd₂Fe₁₄B. The Curie temperature is 585 K, 602 K, and 639 K for Nd₂Fe₁₄B, Dy₂Fe₁₄B, and Tb₂Fe₁₄B, respectively. In order to maintain high coercivity at elevated operating temperature environments as in hybrid electric vehicle engines, the

addition of large amount of heavy rare earth elements such as Dy or/and Tb is substituted for Nd to increase the Curie temperature [10]. However, the disadvantage of substituting Nd with heavy rare earth elements is that it reduces the remanence of the magnets. This is because they couple anti-ferromagnetically with the Fe in the $\text{RE}_2\text{Fe}_{14}\text{B}$ lattice [1, 7]. In addition, availability of heavy rare earth elements on the free market is currently threatened [11]. Therefore, efforts have been initiated to produce heavy rare earth lean magnets that have large coercivity, and good high temperature energy product [12-15]. The idea is to enrich the grain surfaces with heavy rare earth while the core of the grain remains relatively free of heavy rare earth. This would locally increase the anisotropy of the magnet at the point where domain nucleation is easiest. In other words, the basis of this philosophy is to put the heavy rare earth where it is needed the most to decrease the propensity for domain nucleation in reversing fields (Figure 1.2).

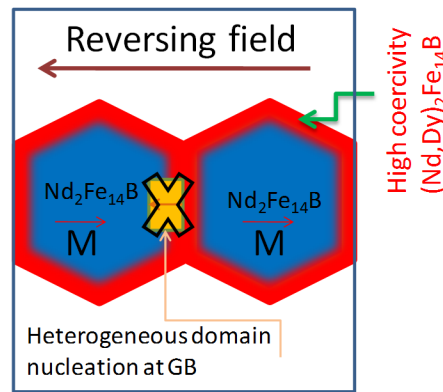


Figure 1.2 Proposal for lean rare earth, high coercivity, high temperature Nd-Fe-B based magnets using grain surface enrichment with heavy rare earth.

Recently, a materials processing approach for grain surface enrichment has been developed [8] (Figure 1.3). Vapor deposition or chemical coatings of Dy on the surface of bulk Nd-Fe-B sintered magnets [16-24] is followed by a diffusion process to introduce Dy on the grain boundaries regions. This grain boundary diffusion processing (GBDP) has been the subject of multiple patents which show a larger than expected increase in coercivity than is expected from the amount of Dy introduced. It has been demonstrated that under the appropriate time and temperature for processing, the Dy penetration along the grain boundary is much greater than the penetration of Dy into the bulk, and the grain surfaces are enriched through much of the magnet thickness. This process can approximate a core-shell structure with $(\text{Nd,Dy})_2\text{Fe}_{14}\text{B}$ in the shell and $\text{Nd}_2\text{Fe}_{14}\text{B}$ in the core. The Dy rich shell is supposed to reduce the efficiency of reverse domain nucleation at the grain surface, even at high temperature.

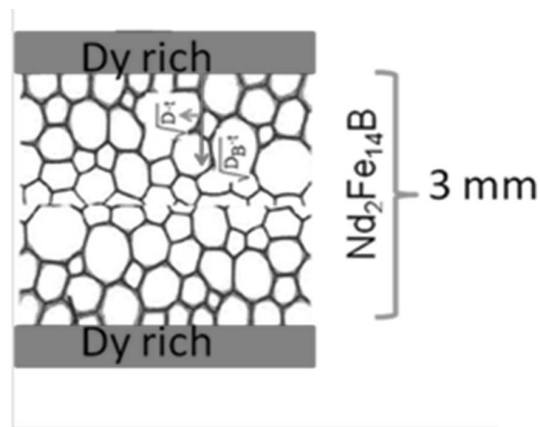


Figure 1.3 The illustration of the core-shell structure of Dy covered $\text{Nd}_2\text{Fe}_{14}\text{B}$ grains.

The issue with the vapor phase coating/GBDP is the cost. GM estimates the equipment investment is on the order of \$10 M. A more efficient manufacturing process than Dy diffusion into bulk magnets from a surface layer would be to produce the core shell structure during sintering rather than after consolidation using a two alloy sintering process where the pellet is formed by blended powders of a Dy rich phase and an Nd rich phase. This has proved problematic.

"With the conventional Two Alloy Method, since the dysprosium is diffused during sintering at high temperatures, the dysprosium is distributed widely in the interior of grains, and so an excess of dysprosium is necessary" [24]

The purpose of this work is to examine the Dy transport in blended powder pellets that are associated with Dy homogenization, and to test the hypothesis that Dy transport efficiency is due to a coupling of liquid diffusion and solution:precipitation processes.

1.1 Background

This project will consider transport behavior in the system Fe-Nd-Dy-B. There is no quaternary phase diagram published for this alloy system. However, all reports to date (references) suggest that the heavy rare earths, such as Dy, form a quasi-binary solution with $\text{Nd}_2\text{Fe}_{14}\text{B}$. That is, there is a solid solution with the two end members $\text{Nd}_2\text{Fe}_{14}\text{B}$ and $\text{Dy}_2\text{Fe}_{14}\text{B}$ and the intermediate concentrations can be represented as $(\text{Nd}_a\text{Dy}_{1-a})_2\text{Fe}_{14}\text{B}$. There is some published data on the solid state volume diffusion coefficient. Compos et

al.[25] has reported that the parameters for Dy diffusion in the $(\text{Nd}_a\text{Dy}_{1-a})_2\text{Fe}_{14}\text{B}$ alloy as 315 kJ/mol for the activation energy (Q) and a D_0 of $8 \times 10^{-4} \text{ m}^2/\text{s}$ to be used in the expression for the volume diffusion coefficient, D, as

$$D = D_0 \exp(-Q/RT) \quad (1.1)$$

Where R is the Gas Constant

There is no published data for the grain boundary diffusion coefficient, but a useful approximation is that $Q_{\text{grain boundary}} \sim 2/3 Q_{\text{volume}}$ [26] [27]. In addition to grain boundary diffusion, it is noted that the liquid phase sintered materials have a significant volume fraction of liquid (>1%) that resides on the grain triple junctions and possibly wets some grain boundaries Figure 1.4 [28].

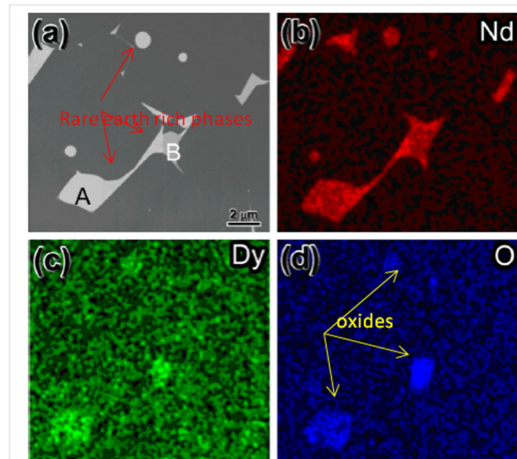


Figure 1.4 (a) Back scattered image showing rare earth rich phases (bright) associated with the eutectic liquid solidification. (b-d) EDS Element maps for Nd, Dy and O. (Figure adapted by author from [28])

The configuration of the liquid phase above the eutectic temperature has been considered by J. J. Fidler and T. Schrefl [29].

"Two conditions must be fulfilled for a complete surrounding of the hard magnetic grains. First, the dihedral angle which was found to be in the order to 10° – 30° and decreases with the amount of doping must become zero. Second, the volume fraction of the liquid phase during sintering must exceed a certain value $\sim 20\%$!. Both criteria are not fulfilled in Nd–Fe–B magnets. Thus, the typical microstructure consists of two types of grain boundaries, one containing intergranular phases especially at grain junctions and corners and one in direct contact to each other." Thus, the transport along the 'grain boundary' can be influenced by transport through the liquid phase, especially along interconnected grain boundary triple junctions and grain corners. This is important because the diffusion coefficient for liquid phase diffusion could be as low as $10^{-5} \text{ cm}^2/\text{s}$. The diffusion coefficients for volume diffusion, grain boundary diffusion (approximate) and liquid phase diffusion (of rare earth in heavy metal melt) are compared in Figure 1.5,

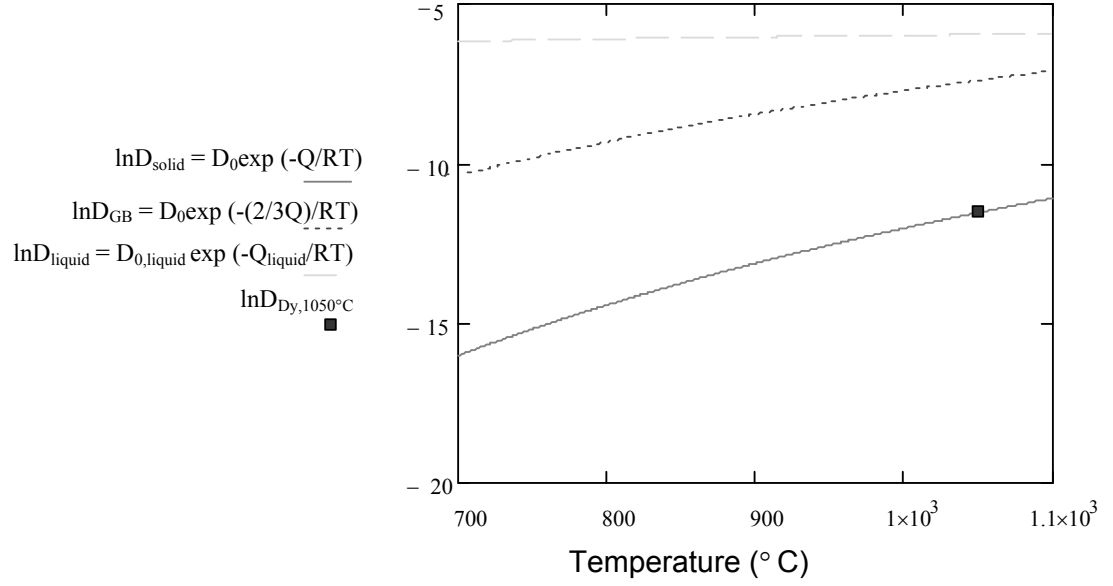


Figure 1.5 Diffusion coefficients for volume diffusion, grain boundary diffusion, liquid phase diffusion, and diffusion of Dy at 1050°C

The effective diffusion coefficient for liquid phase diffusion in a microstructure of 97-99% solid would also depend on the volume fraction of the liquid (ϵ) and tortuosity (τ) of liquid phase 'pipes' lying along grain edges, corners and triple junctions. That is, in porous materials, the diffusion coefficient of a liquid phase is modulated by the pore fraction, ϵ , and tortuosity through the expression [30]

$$D_{\text{porous}} = \frac{D_{\text{liquid}} * \epsilon}{\tau} \quad (1.2)$$

This suggests that the observed diffusion coefficient in the liquid could be reduced by two to three orders of magnitude compared to liquid diffusion in non-porous systems.

In the two alloy method and surface coating method for GBDP, the process introduces a new liquid composition which is not (initially) in equilibrium with the bulk composition. The introduction of Dy into the Nd rich eutectic liquid during the GBDP will result in an increase in ‘a’ for the $(\text{Nd}_a\text{Dy}_{1-a})_2\text{Fe}_{14}\text{B}$ phase in contact with the liquid. One possibility is that the composition change will occur by solid state diffusion from the grain surfaces in contact with the liquid. Our experimental observations will also suggest a second possibility, namely that the nonequilibrium conditions between the solid and the liquid will result in the solid being dissolved by the liquid, followed by a reprecipitation of a new solid having a composition equal to that required by equilibrium. The dissolution:reprecipitation process driven by the Gibbs-Thompson effect is well known in liquid phase sintering as a mechanism of grain coarsening [31], but due to the non-equilibrium between the liquid and the bulk of the solid, dissolution:reprecipitation driven by free energy of mixing must also be considered [32].

Nourtier-Mazauric et. al.[32] consider an ideal solid solution not in equilibrium with a surrounding liquid for a ternary (or higher) system. They find “*The kinetic behavior of an ideal solid solution is modelled by two competing reactions: the stoichiometric dissolution of the existing solid and the precipitation of the least soluble compound, i.e. that with respect to which the oversaturation of the liquid is maximum... The model accounts well for the tendency of solid solutions to dissolve congruently before precipitation starts and drives the liquid composition towards equilibrium.*”

In the two-alloy method, Dy rich powder is mixed with Nd rich powder that will form a eutectic liquid. The eutectic liquid in equilibrium with the $\text{Nd}_2\text{Fe}_{14}\text{B}$ will not initially be in equilibrium with the Dy rich phase. This sets up the possibility of dissolution of the Dy rich phase and reprecipitation of a $(\text{Nd}_a\text{Dy}_{1-a})_2\text{Fe}_{14}\text{B}$ phase. Alternatively, if Dy rich liquid is produced during the processing, this liquid may dissolve the $\text{Nd}_2\text{Fe}_{14}\text{B}$ phase and reprecipitate a $(\text{Nd}_a\text{Dy}_{1-a})_2\text{Fe}_{14}\text{B}$ phase. Since the mass transport in a dissolution:reprecipitation process occurs via a liquid phase, this may be a much more efficient process for Dy composition homogenization than solid state diffusion.

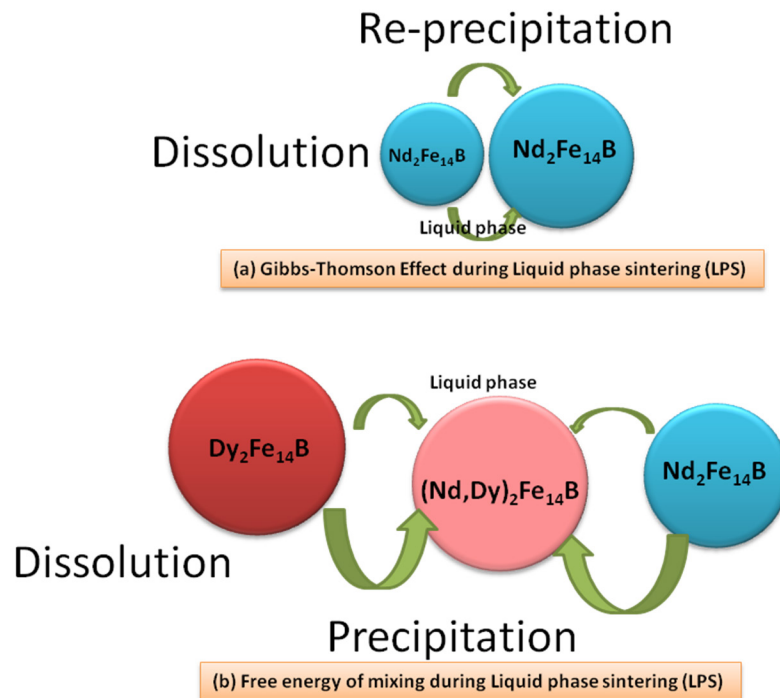


Figure 1.6 (a) Dissolution:reprecipitation driven by Gibbs-Thompson Effect (b) dissolution:reprecipitation driven by free energy of mixing.

Chapter 2

Experimental Procedure

The initial experiment of Dy diffusion in the Nd-Fe-B material was investigated by powder metallurgy method. In this process, a sintered pellet of mixed $\text{Dy}_2\text{Fe}_{14}\text{B}$ flakes and $\text{Nd}_2\text{Fe}_{14}\text{B}$ powder was studied. The scanning electron microscope was employed to observe the post-sintering sample morphology. We found that the Nd rich liquid phase was aggressive attacked into the $\text{Dy}_2\text{Fe}_{14}\text{B}$ flakes during the heat treatment process. There was no eutectic phase around the $\text{Nd}_2\text{Fe}_{14}\text{B}$ grains that could be observed. Therefore, a macroscopic transportation of Dy rich liquid diffusion lengths through connected porosity in the sintered layered-pellets was studied to be able to explain its diffusion mechanism. The reaction between Dy and $\text{Nd}_2\text{Fe}_{14}\text{B}$ phase was also investigated by the microstructure study of the reaction between Dy-Fe eutectic coating and $\text{Nd}_{2.7}\text{Fe}_{14}\text{B}_{1.4}$ ribbons. The dissolution-precipitation process between solid and liquid phases was proposed to explain the reaction.

2.1 Diffusion of Dy in $\text{Nd}_2\text{Fe}_{14}\text{B}$ composition

Small pieces of commercial $\text{Nd}_{2.7}\text{Fe}_{14}\text{B}_{1.4}$ bulk ingots were melted and casted into ribbons by melt spinning process under argon atmosphere with a wheel speed of 20 meters per second. The $\text{Nd}_{2.7}\text{Fe}_{14}\text{B}_{1.4}$ ribbons were milled in spex milling machine in a glove box for 15 minutes with two of half inch steel balls. Rare earth magnets can be very sensitive to the environment as the rare earth reacts strongly with oxygen due to

their very low free energy of transformation ($\Delta G_f \text{Nd}_2\text{O}_3(298.15 \text{ K})$ is -1721.049 kJ/mol , $\Delta G_f \text{Dy}_2\text{O}_3(298.15 \text{ K})$ is -1771.359 kJ/mol) [33]. The oxidation causes the precipitation of Fe ($\Delta G_f \text{Fe}_2\text{O}_3(298.15 \text{ K})$ is -742.294 kJ/mol) at the surface of $\text{Nd}_2\text{Fe}_{14}\text{B}$ grains. Therefore, the precipitation of the oxygen at low ppm will result in decreasing coercivity of material[1]. This requires great care in the production and sample preparation for metallurgical study.

$\text{Dy}_2\text{Fe}_{14}\text{B}$ with 2 at% extra B flakes were produced from arc melted 13 gm $\text{Dy}_{2.34}\text{Fe}$ with 25.77 gm Fe and 0.51 gm B powder. The melted alloys were remelted and casted into ribbon form by melt spinning. The processing condition used to produce the ribbons was as same as $\text{Nd}_{2.7}\text{Fe}_{14}\text{B}_{1.4}$ ribbons. The ribbons were milled for 50 minutes with a 0.25 inch diameter steel ball in spex mill in a glove box to avoid air contact. After milling both composition separately, they were mixed together in spex milling without grinding media for 15 minutes. The obtained 5 wt% Dy composition powder with small flakes was pressed at 422 Mpa and held for 3 minutes. The pressed pellet was sintered in vacuum furnace by two steps sintering. The first step was at 850°C for 10 hours then directly heated up to 1050°C and held for 30 minutes. The cooling rate was on the furnace.

The microstructure of sintered pellet was observed by scanning electron microscope (SEM). The element compositions in the eutectic or Nd rich phase and some

areas were collected by energy dispersive spectroscopy (EDS) analysis with the standardless analysis from Revolution® software.

2.2 Dy Transport Control during the Sintering Process

The liquid phase in the powder pack of $\text{Nd}_{2.7}\text{Fe}_{14}\text{B}_{1.4}$ was studied in order to control the capability of the liquid phase that occurred during the sintering process and effect to the magnetic property of the $\text{Nd}_2\text{Fe}_{14}\text{B}$ magnets. The three layered pellets that added 30% $\text{Dy}_{2.34}\text{Fe}$ plus 70% $\text{Nd}_2\text{Fe}_{14}\text{B}$, 30% $\text{Dy}_{2.34}\text{Fe}$ plus 70% $\text{Nd}_2\text{Fe}_{14}\text{B}$ plus 1.5 mole Fe_{14}B per mole Nd liquid in $\text{Nd}_2\text{Fe}_{14}\text{B}$ magnets, and $\text{Dy}_2\text{Fe}_{14}\text{B}$ plus 2 at% extra boron powder into the center of $\text{Nd}_{2.7}\text{Fe}_{14}\text{B}_{1.4}$ powder pack for each pellet were investigated the transportation of Dy during the sintering.

2.2.1 Preparation of layered pellets

The commercial $\text{Nd}_{2.7}\text{Fe}_{14}\text{B}_{1.4}$ alloy powder from GreatWestern Technologies Inc. was used as a Nd-Fe-B source in the powder pack. The chemical composition of as-cast alloy was determined using inductively coupled plasma analysis (ICP) as shown in Table 2.1.

Table 2.1 Chemical composition of Nd_{2.7}Fe₁₄B_{1.4} alloy powder

Element	Weight percent
Iron	65.76
Neodymium	32.99
Boron	1.25
Impurities	
Praseodymium	0.130
Aluminum	0.025
Chromium	0.002
Magnesium	< 0.001
Manganese	< 0.009
Silicon	0.033
Carbon	0.008
Oxygen	0.012

Dy_{2.34}Fe ribbons were produced from the commercial Dy_{2.34}Fe ingots as the starting materials by using melt-spinning machine. The alloy ingots were melted and casted on the copper wheel under argon atmosphere with the optimal wheel speed 20 m/s. These Dy_{2.34}Fe ribbons were milled with another alloy to make new compositions for the center layer of the pellets.

The three mixing alloy powders for the center layer of the pellets were prepared in a glove box under argon atmosphere by using spex-milling process described as follow.

In a first alloy powder composition, the mixed 30%Dy_{2.34}Fe plus 70% Nd₂Fe₁₄B powder was prepared by milling 3.6 gm Dy_{2.34}Fe and 8.4 gm Nd₂Fe₁₄B in a spex mill

grinder for 30 minutes with two of half-inch steel balls. A second alloy powder composition, the mixed 30% $\text{Dy}_{2.34}\text{Fe}$ plus 70% $\text{Nd}_2\text{Fe}_{14}\text{B}$ plus 1.5 mole Fe_{14}B per mole Nd liquid in $\text{Nd}_2\text{Fe}_{14}\text{B}$ magnets was prepared by mixing 2 gm of 30% $\text{Dy}_{2.34}\text{Fe}$ plus 70% $\text{Nd}_2\text{Fe}_{14}\text{B}$ alloy powder with 2.7 gm Fe powder and approximately 0.037 gm B powder in the spex mill with two of half-inch steel balls for 15 minutes. A third alloy powder composition, 13 gm $\text{Dy}_{2.34}\text{Fe}$ with 25.77 gm Fe and 0.51 gm B powder were homogenized by arc melting technique. Then, the melt spinning method was employed to produce $\text{Dy}_2\text{Fe}_{14}\text{B}$ plus 2 at% extra boron ribbons. These ribbons were milled by spex mill with two of half-inch steel balls for 15 minutes.

Three layered-pellets were pressed at 422 MPa and held for 3 minutes by a cold hydraulic pressing under argon atmosphere. The approximately 7 gm $\text{Nd}_{2.7}\text{Fe}_{14}\text{B}_{1.4}$ alloy powder was put into the half-inch cylindrical split die. Then, about 1.7 gm prepared alloy powder for the center layer was added into the die. After that, the 7 gm $\text{Nd}_{2.7}\text{Fe}_{14}\text{B}_{1.4}$ alloy powder was added for the top layer. The illustration of the layered pellets is shown in Figure 2.1.

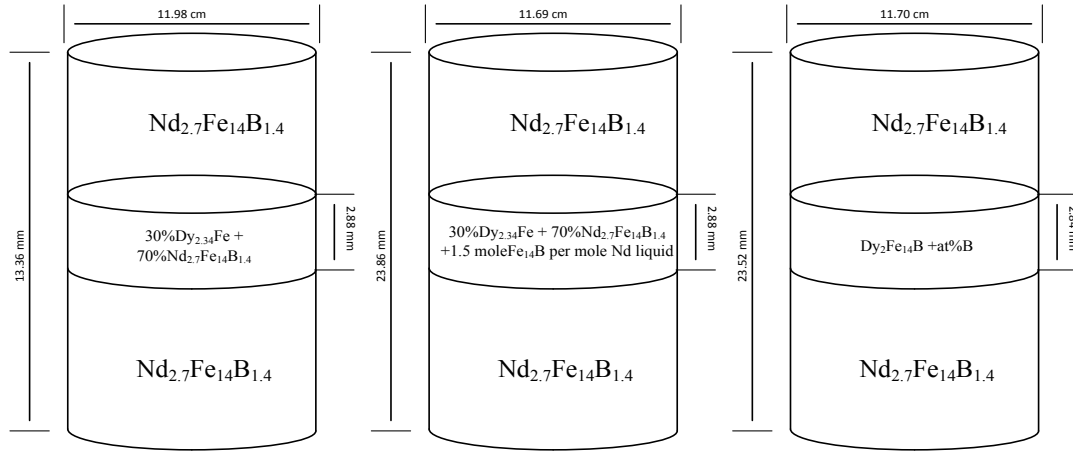


Figure 2.1 The illustration of three layered pellets.

The three layered-pellets were sintered in vacuum furnace at 950°C with $7^{\circ}\text{C}/\text{min}$ average heating rate. The pellets were held at the sintering temperature for 5 hours. The sintered layered-pellet samples were ground by silicon carbide abrasive papers from grit size number 120, 240, 320, 400, and 600. Then, they were polished with $5\text{ }\mu\text{m}$ silicon carbide polishing paper and $0.05\text{ }\mu\text{m}$ alumina particles, respectively. The polished samples were washed in an ultrasonic with purified ethanol, then, dried by using cold air.

2.2.2 Characterization of the layered-pellets

The qualitative and quantitative elemental analyses of the polished layered-pellets were determined by using the energy dispersive spectroscopy (EDS) analysis that was intergraded with the Revolution® software. The Dy concentration at each depth away from the center layer was collected to determine the amount of Dy that can be diffused away from the Dy source. National Institute of Standards and Technology (NIST)

standards were used for Dy, Nd, and Fe that known purity were applied as reference materials. A known composition of $\text{Nd}_2\text{Fe}_{14}\text{B}$ magnet was used as a standard sample.

The weight percent of Dy element at 50, 100, 350, 600, 850, and 1000 μm -depth away from the center layer were collected. At each depth, three areas of the amount of Dy in the eutectic phase and solid phase that far away from the eutectic phase about 1-2 μm were determined. The illustration of the collecting areas was presented in Figure 2.2. The morphology of the samples were observed by using scanning electron microscope (SEM) with back-scattered electrons (BSE).

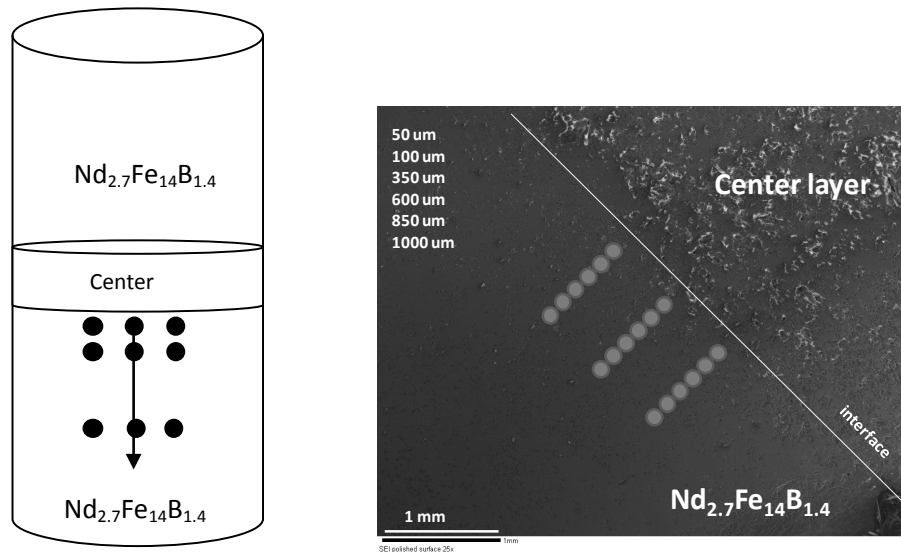


Figure 2.2 The illustration shows the points were collected from the layered pellet.

2.3 The Eutectic liquid and the solid reaction study

2.3.1 Dy-Coated ribbons preparation

The small $\text{Dy}_{2.34}\text{Fe}$ alloy pieces were used as the source of Dy coating on the surface of melt spun $\text{Nd}_{2.7}\text{Fe}_{14}\text{B}_{1.4}$ ribbons via a Physical Vapor Deposition process (PVD). The schematic of this process is illustrated in Figure 2.3. The Dy-coated on $\text{Nd}_{2.7}\text{Fe}_{14}\text{B}_{1.4}$ ribbons were heated at 850°C and 950°C in the vacuum condition with one-hour holding time.

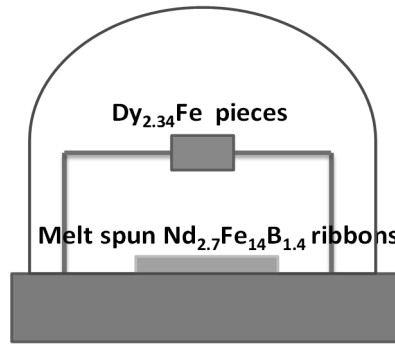


Figure 2.3 Schematic representation of Physical Vapor Deposition process.

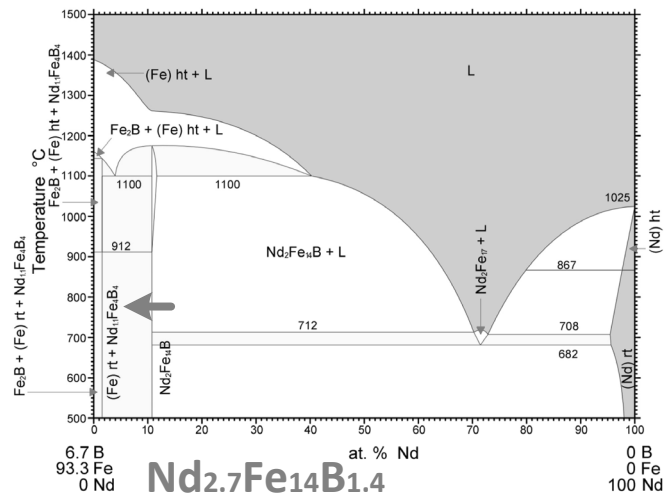
2.3.2 Characterization of Dy-Coated ribbons

A cold field emission high resolution scanning electron microscope (FE-SEM) with integrated EDS system was used to examine the morphology, qualitative and quantitative elemental analyses, and measure the film thickness.

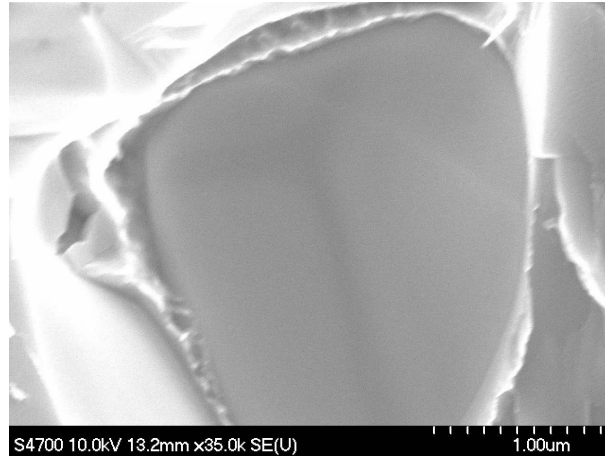
Chapter 3

Results and discussions

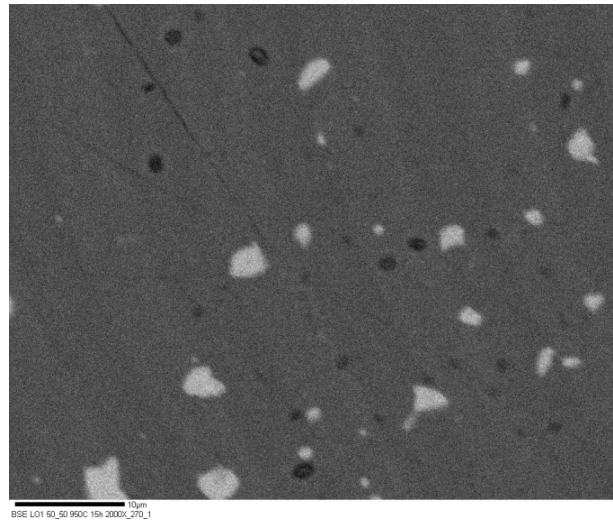
In this work, we report on the study of the Dy transport in $\text{Nd}_{2.7}\text{Fe}_{14}\text{B}_{1.4}$ powder pack that are non-homogeneous with respect to Dy. This is a multicomponent, two-phase system ($\text{RE}_2\text{Fe}_{14}\text{B} + \text{eutectic liquid}$) at the consolidation temperature as shown in the isopleths of the Nd-Fe-B ternary phase diagram in Figure 3.1(a). This structure of two-phase system is shown in Figure 3.1 (b) and (c), where the rare earth rich eutectic phase can be observed. The transport process is complicated by the relatively high transport efficiency in the liquid phase relative to the solid phase. In addition, the possibility of solid dissolution:reprecipitation will be considered as a mechanism of Dy homogenization.



(a)



(b)



(c)

Figure 3.1 (a) The Nd-Fe-B ternary phase diagram [5] , (b) Nd-Fe-B sintered two phase structure with RE rich eutectic phase seen as the ductile phase at the grain boundary in the fracture surface cross section. (c) Nd-Fe-B sintered two phases structure with RE rich eutectic phase shown as bright in the BSE polished surface.

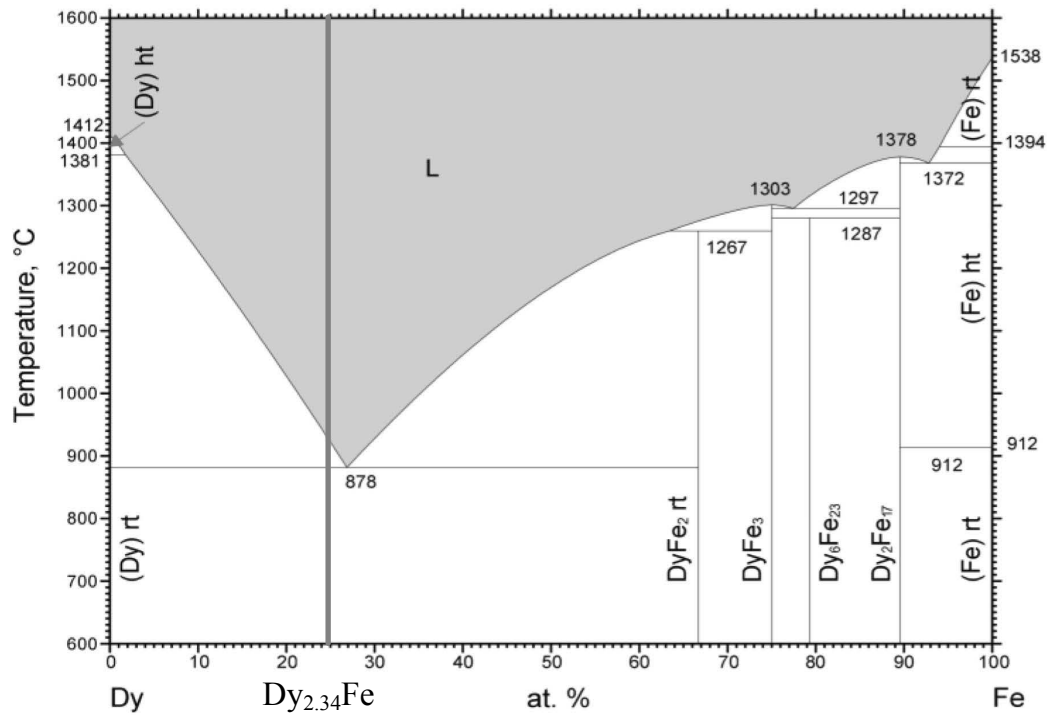
3.1 Dy Transport Control during the Sintering Process

3.1.1 Increasing the melting point and spacing of the Dy source

As indicated in figure 3.2, the Dy-Fe phase diagram shows a eutectic temperature at 878°C. At this temperature, compositions between Dy and DyFe₂ produce a liquid phase. The composition that of interest to this study is Dy_{2.34}Fe (eutectic composition is Dy₃Fe). The liquid phase forming at this composition at the eutectic temperature has a composition that is 70 atomic percent. This material is added to the Nd_{2.7}Fe₁₄B_{1.4} powder pack to produce a high concentration of Dy atoms in the liquid phase to penetrate along the Nd₂Fe₁₄B grain boundaries through the connected pore. The ability to produce a high volume of material with grain surfaces enriched in Dy requires that the transport efficiency of Dy from the liquid into the solid be small compared to the transport efficiency of Dy in the liquid phase along the boundaries/pores. The basic concept may be illustrated by assuming all boundary layer transport is controlled by diffusion through the boundary liquid with diffusivity (D_B) and all transport through the solid is by diffusion with volume diffusivity (D), then grain surface enrichment throughout the powder pack requires (by analogy with the Biot number)

$$\frac{\sqrt{D \cdot t}}{G} \cdot \frac{L}{\sqrt{D_B \cdot t}} < 0.1 \quad (3.1)$$

Where L is the distance between Dy sources and G is the grain size.



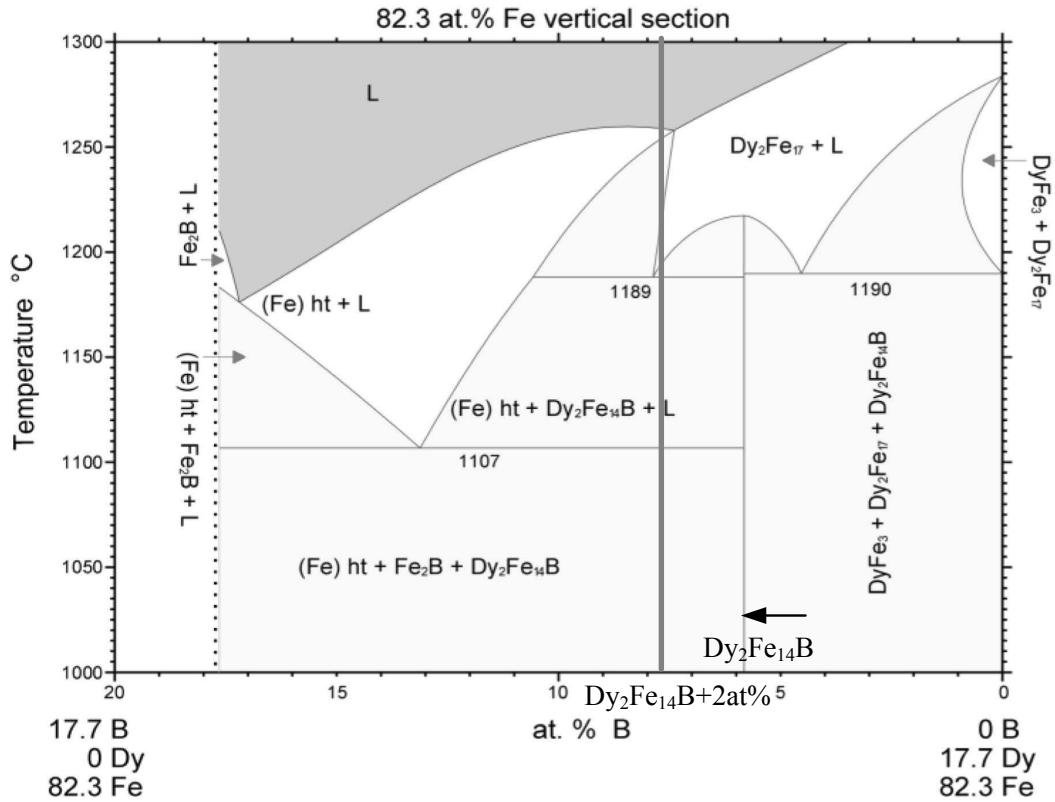
© ASM International 2006. Diagram No. 981146

Figure 3.2 Dy-Fe binary phase diagram [34]

The use of a Dy:Fe alloy at composition close to the eutectic composition results in a large liquid phase infusion into the powder pack at a temperature below the consolidation temperature. Limitation of the liquid phase volume increase can be controlled by introduction of higher melting point, Dy rich compounds into the powder pack. The Dy liquid phase transport capability is then controlled by the interaction of a solid Dy rich phase with the Nd rich eutectic phase.

3.1.2 High melting point Dy source.

The $\text{Dy}_2\text{Fe}_{14}\text{B}$ is considered a candidate to use as the new Dy source due to its high melting temperature. According to the Dy-Fe-B ternary phase diagram (Figure 3.3), the eutectic temperature for $\text{Dy}_2\text{Fe}_{14}\text{B}$ with additional boron is 1107°C , which is above the highest reported consolidation temperature of 1050°C . Therefore, $\text{Dy}_2\text{Fe}_{14}\text{B}$ plus 2 at%B exhibits higher melting point than $\text{Dy}_{2.34}\text{Fe}$.



© ASM International 2006. Diagram No. 977949

Figure 3.3 Dy-Fe-B phase diagram [35]

3.1.3 Schematic of transient liquid sintering

The 30% $\text{Dy}_{2.34}\text{Fe}$ plus 1.5 mole Fe_{14}B per mole of Nd liquid forces a reaction between the rare earth rich eutectic phase and the Fe_{14}B powder during the liquid phase transport process. This transient liquid phase sintering process is carried out in order to reduce the liquid phase volume fraction over the time of the experiment. As shown in the Nd-Fe-B ternary phase diagram (Figure 3.4), $\text{Nd}_{2.7}\text{Fe}_{14}\text{B}_{1.4}$ starts melting at 682°C and $\text{Dy}_{2.34}\text{Fe}$ begins melting at 878°C as presented in Figure 3.2. In consideration for reducing the amount of liquid phase, the excess of Fe_{14}B is used for limiting the lifetime of Nd-Dy rich liquid phase throughout the sintering process. The excess Fe_{14}B powder will drive the average composition toward the stoichiometric 2:14 compound. The schematic in Figure 3.5 illustrates this purpose mechanism of excess Fe_{14}B powder. The rare earth liquid phase (Nd-Dy liquid phase which Nd rich liquid composition) occurs after the $\text{Nd}_{2.7}\text{Fe}_{14}\text{B}_{1.4}$ melting point. The Nd rich liquid is moved into Fe_{14}B powder and transformed to $\text{Nd}_{2.7}\text{Fe}_{14}\text{B}_{1.4}$ that has higher melting point than $\text{Dy}_{2.34}\text{Fe}$. Therefore, the existence of Nd rich liquid can be controlled.

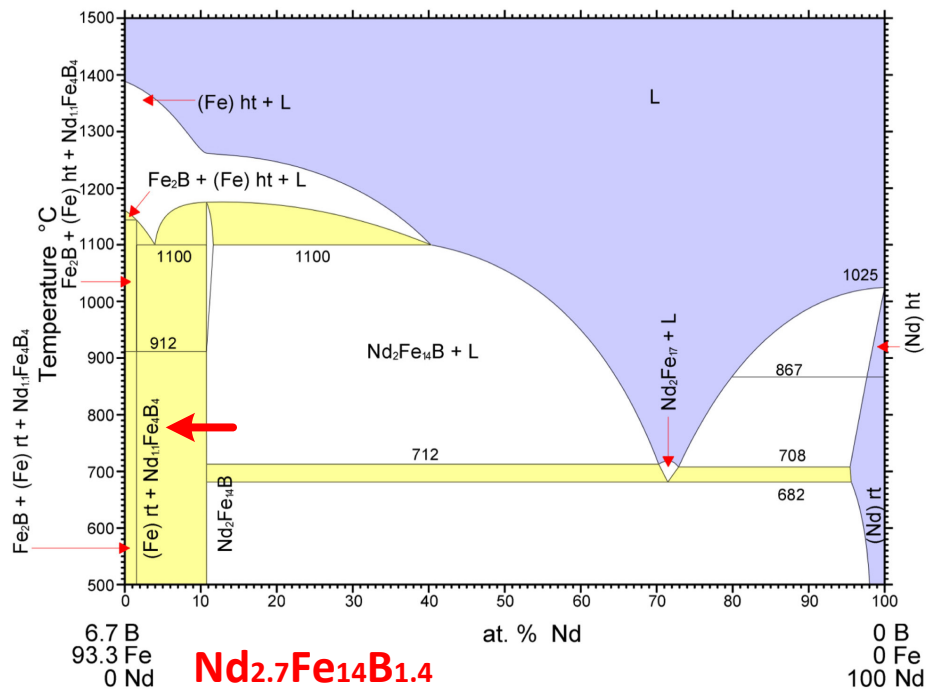


Figure 3.4 The ternary Nd-Fe-B phase diagram [5]

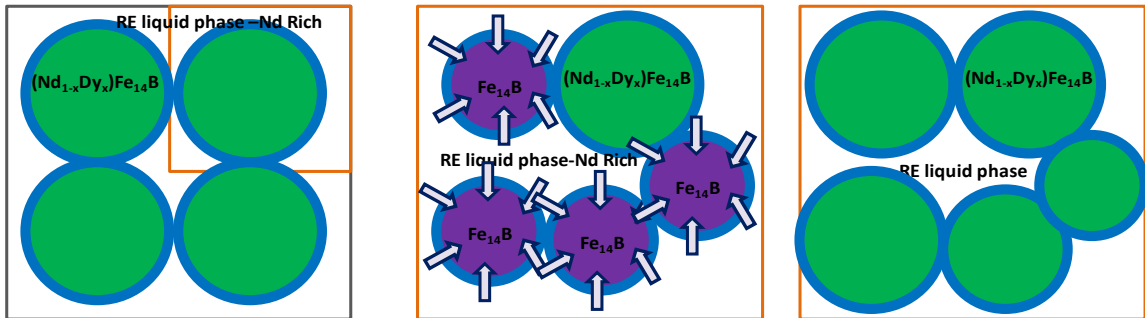
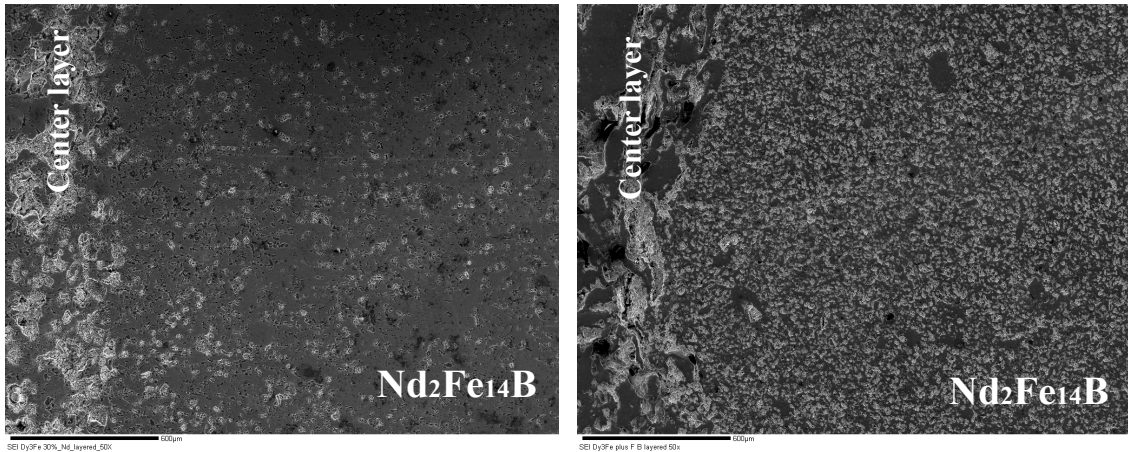


Figure 3.5 The schematic shows Fe₁₄B and Nd rich liquid mechanism

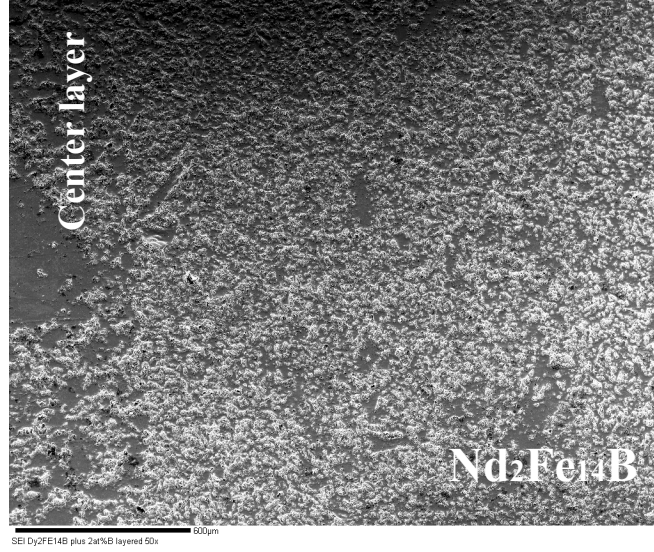
3.1.4 Layer pellet microstructure

The sintered pellets of the three layered pellets was fabricated as described in Chapter 2. The SEM and EDS analysis were carried out to study the transport mechanism of Dy sources. The SEM images in SEI mode at low magnification was captured for observing the overall morphology and represented porosity of the layered pellets. The SEM images of $\text{Nd}_{2.7}\text{Fe}_{14}\text{B}_{1.4}/30\%\text{Dy}_{2.34}\text{Fe}/\text{Nd}_{2.7}\text{Fe}_{14}\text{B}_{1.4}$ pellet, $\text{Nd}_{2.7}\text{Fe}_{14}\text{B}_{1.4}/30\%\text{Dy}_{2.34}\text{Fe}$ plus 1.5 Mole Fe_{14}B per mole of Nd liquid mixing powder/ $\text{Nd}_{2.7}\text{Fe}_{14}\text{B}_{1.4}$ pellet, and $\text{Nd}_{2.7}\text{Fe}_{14}\text{B}_{1.4}/\text{Dy}_2\text{Fe}_{14}\text{B}$ plus 2at% B/ $\text{Nd}_{2.7}\text{Fe}_{14}\text{B}_{1.4}$ pellet show in Figure 3.6. The $\text{Nd}_{2.7}\text{Fe}_{14}\text{B}_{1.4}$ layer in $\text{Nd}_{2.7}\text{Fe}_{14}\text{B}_{1.4}/30\%\text{Dy}_{2.34}\text{Fe}/\text{Nd}_{2.7}\text{Fe}_{14}\text{B}_{1.4}$ pellet (Figure 3.6 (a)) shows less porosity than 30%Dy_{2.34}Fe at the center layer. In contrast, $\text{Nd}_{2.7}\text{Fe}_{14}\text{B}_{1.4}$ layer in $\text{Nd}_{2.7}\text{Fe}_{14}\text{B}_{1.4}/30\%\text{Dy}_{2.34}\text{Fe}$ plus 1.5 mole Fe_{14}B per mole of Nd liquid mixing powder/ $\text{Nd}_{2.7}\text{Fe}_{14}\text{B}_{1.4}$ pellet (Figure 3.6 (b)), and $\text{Nd}_{2.7}\text{Fe}_{14}\text{B}_{1.4}/\text{Dy}_2\text{Fe}_{14}\text{B}$ plus 2at%B/ $\text{Nd}_{2.7}\text{Fe}_{14}\text{B}_{1.4}$ pellet (Figure 3.6 (c)) illustrate that the samples have very high volume of porosity.



(a)

(b)



(c)

Figure 3.6 SEM images in SEI mode at low magnification of $\text{Nd}_{2.7}\text{Fe}_{14}\text{B}_{1.4}$ /30% $\text{Dy}_{2.34}\text{Fe}$ / $\text{Nd}_{2.7}\text{Fe}_{14}\text{B}_{1.4}$ pellet (a), $\text{Nd}_{2.7}\text{Fe}_{14}\text{B}_{1.4}$ /30% $\text{Dy}_{2.34}\text{Fe}$ plus 1.5 mole Fe_{14}B per mole of Nd liquid mixing powder/ $\text{Nd}_{2.7}\text{Fe}_{14}\text{B}_{1.4}$ pellet (b), and $\text{Nd}_{2.7}\text{Fe}_{14}\text{B}_{1.4}$ / $\text{Dy}_2\text{Fe}_{14}\text{B}$ plus 2at%B/ $\text{Nd}_{2.7}\text{Fe}_{14}\text{B}_{1.4}$ pellet (c).

3.1.4.1 $\text{Nd}_{2.7}\text{Fe}_{14}\text{B}_{1.4}$ /30% $\text{Dy}_{2.34}\text{Fe}$ / $\text{Nd}_{2.7}\text{Fe}_{14}\text{B}_{1.4}$ pellet

The SEM from backscattering mode of the 30% $\text{Dy}_{2.34}\text{Fe}$ center layer is presented in Figure 3.7. It can be seen that the microstructure is nonhomogenous with the clusters of two-phase region. The black regions are pores. The regions of white contrast are the rare earth rich phase (Nd-Dy rich phase). The EDS analysis of identified composition in area A is 49.47 ± 0.33 wt%Fe, 22.28 ± 0.29 wt%Nd, and 28.25 ± 0.64 wt%Dy. The composition of the rare earth rich phase in area C is 10.55 ± 0.27 wt%Fe, 43.22 ± 0.50 wt%Nd, and 46.03 ± 0.99 wt%Dy. Comparison between area A and C, the weight percent of iron in area C is less than area A, but it has very rich in Nd and Dy elements. This

results in the brighter contrast in area C due to the high atomic number of Nd and Dy. The gray regions are indicated as the ferromagnetic phase ($\text{Nd}_2\text{Fe}_{14}\text{B}$) with 74.98 ± 0.36 wt%Fe, 1.25 ± 0.20 wt%Nd, and 12.51 ± 0.36 wt%Dy (area B).

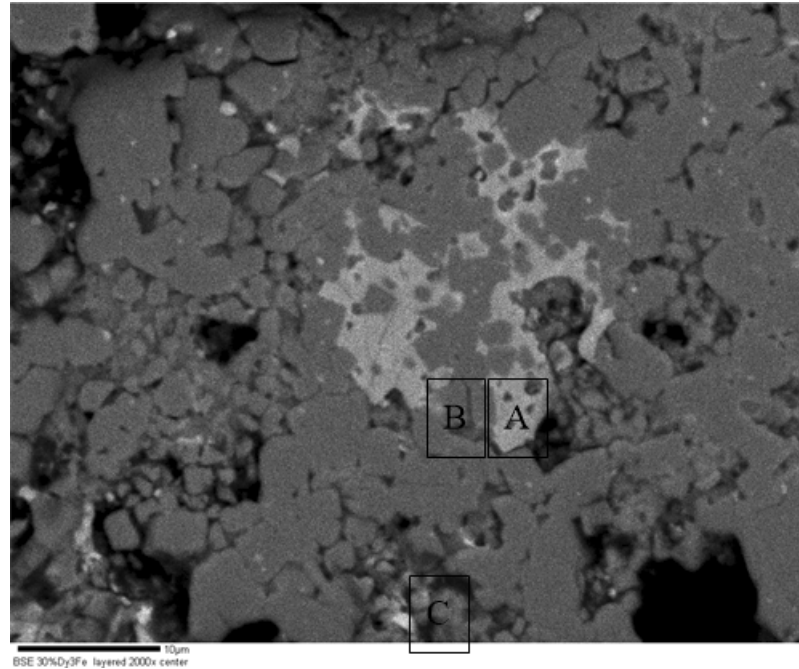
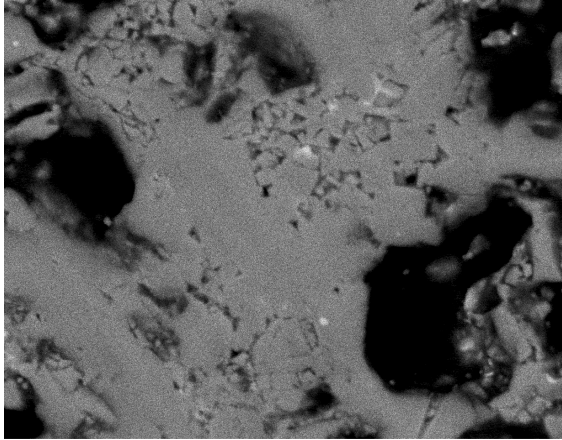
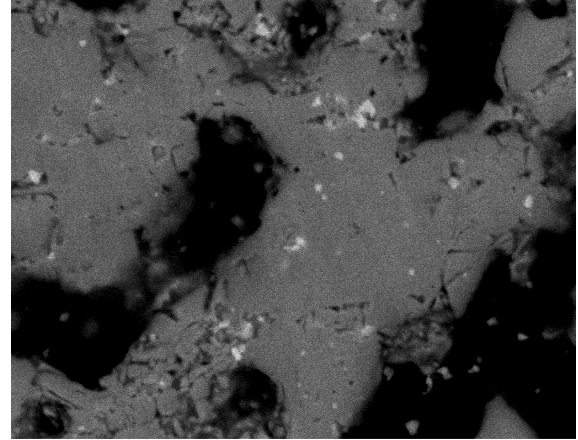


Figure 3.7 SEM image in BSE mode of 30%Dy_{2.34}Fe center layer

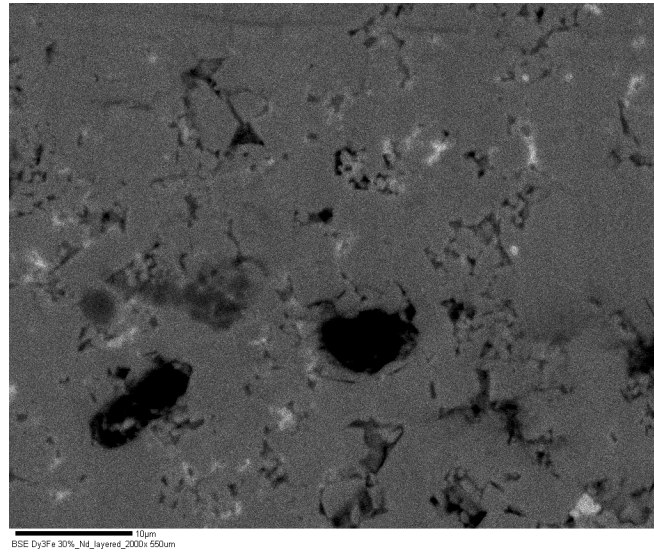
The backscattering images of the two phase region in the $\text{Nd}_2\text{Fe}_{14}\text{B}$ layer are shown in figure 3.8. The Dy composition away from the center layer is presented in Figure 3.9.



(a)



(b)



(c)

Figure 3.8 SEM images in BSE mode of $\text{Nd}_{2.7}\text{Fe}_{14}\text{B}_{1.4}$ layer in $\text{Nd}_{2.7}\text{Fe}_{14}\text{B}_{1.4}/30\%\text{Dy}_{2.34}\text{Fe}/\text{Nd}_{2.7}\text{Fe}_{14}\text{B}_{1.4}$ pellet. At position away from interface 100 μm (a), 350 μm (b), and 550 μm (c).

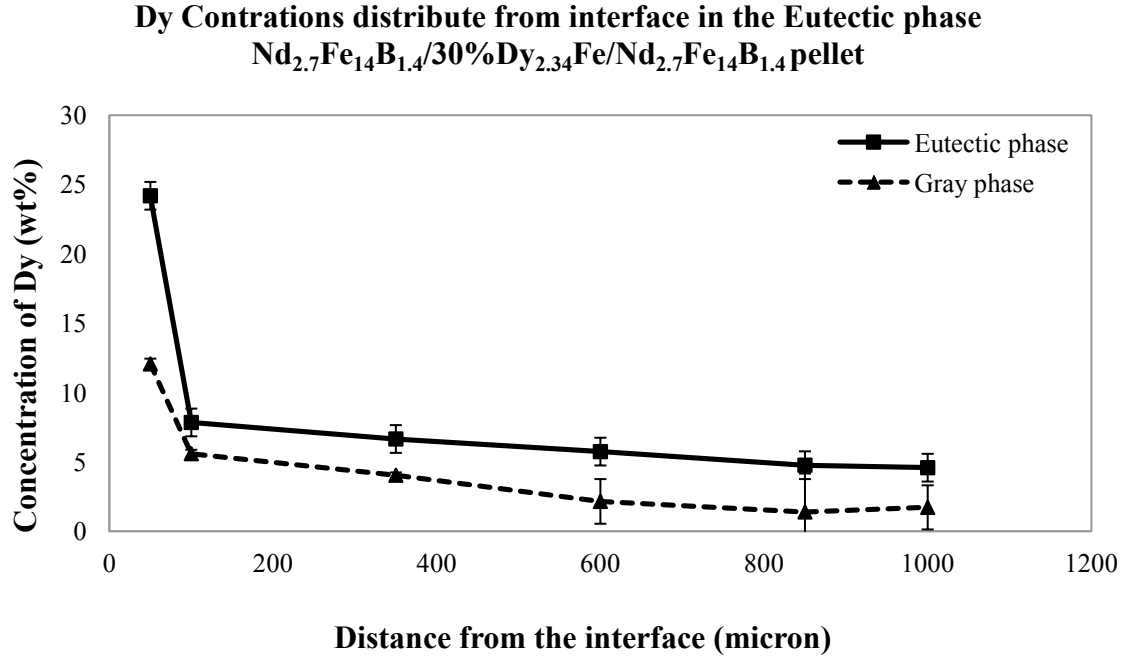


Figure 3.9 The concentration of Dy in eutectic and gray phases of $\text{Nd}_{2.7}\text{Fe}_{14}\text{B}_{1.4}/30\%\text{Dy}_{2.34}\text{Fe}/\text{Nd}_{2.7}\text{Fe}_{14}\text{B}_{1.4}$ pellet at each distance from the center layer

3.1.4.2 $\text{Nd}_{2.7}\text{Fe}_{14}\text{B}_{1.4}/30\%\text{Dy}_{2.34}\text{Fe}$ plus 1.5 Mole Fe_{14}B per mole of Nd liquid mixing powder/ $\text{Nd}_{2.7}\text{Fe}_{14}\text{B}_{1.4}$ pellet

The backscattering images of the 30% $\text{Dy}_{2.34}\text{Fe}$ plus 1.5 Mole Fe_{14}B /Mole of Nd liquid at the center layer is shown in Figure 3.10. The composition in the Nd rich phase in area A is 2.65 ± 0.17 wt%Fe, 79.57 ± 0.73 wt%Nd, and 17.77 ± 0.49 wt%Dy. The gray phase in area B composes of 71.89 ± 0.34 wt%Fe, 22.81 ± 0.27 wt%Nd, and 5.3 ± 0.24 wt%Dy.

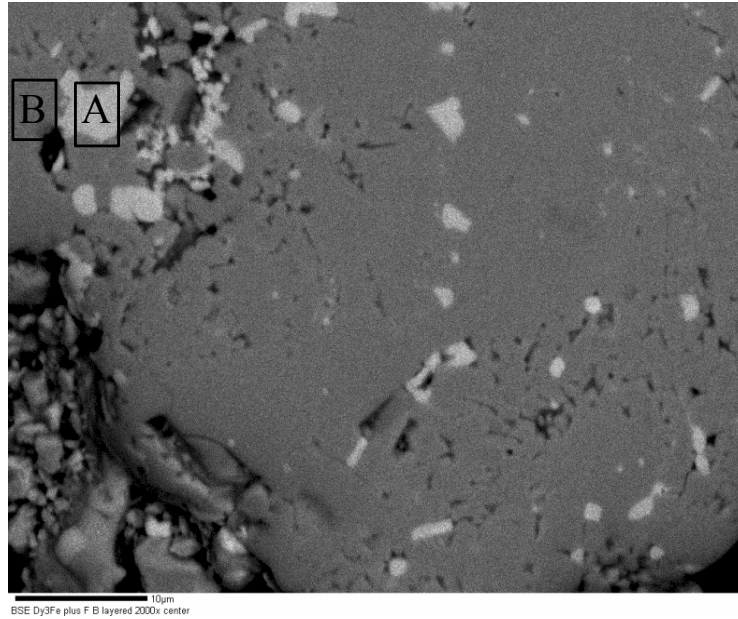
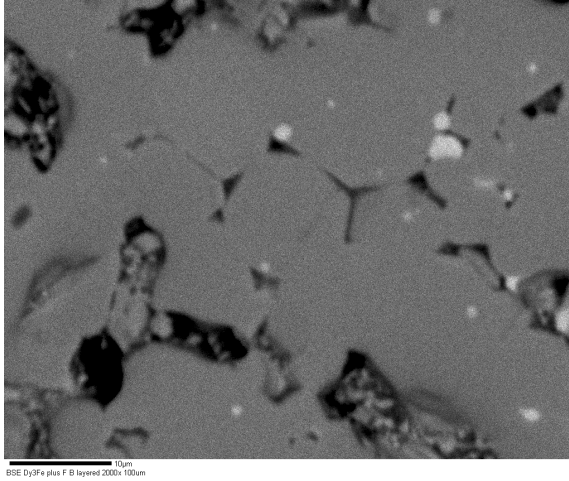
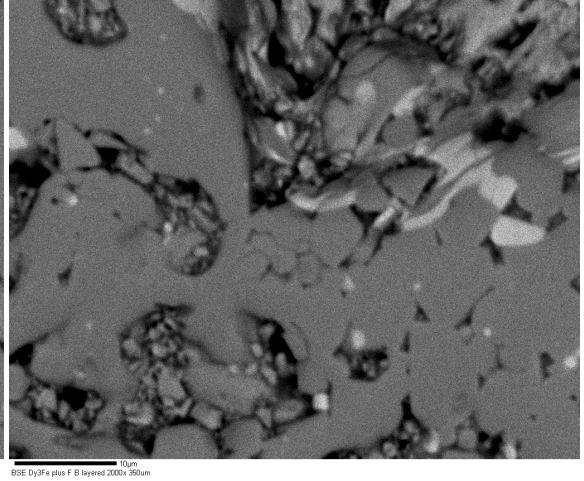


Figure 3.10 SEM image in BSE mode of 30% $\text{Dy}_{2.34}\text{Fe}$ plus 1.5 Mole Fe_{14}B per mole of Nd liquid center layer

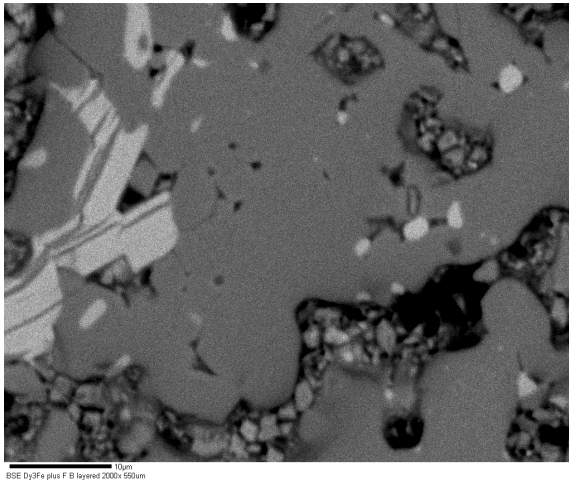
The SEM images in BSE mode in Figure 3.11 (a), (b), (c), and (d) show the microstructure in the $\text{Nd}_2\text{Fe}_{14}\text{B}$ layer with the Nd rich phase and $\text{Nd}_2\text{Fe}_{14}\text{B}$ gray phase. The EDS result for Dy concentration away from the center layer is presented in Figure 3.12.



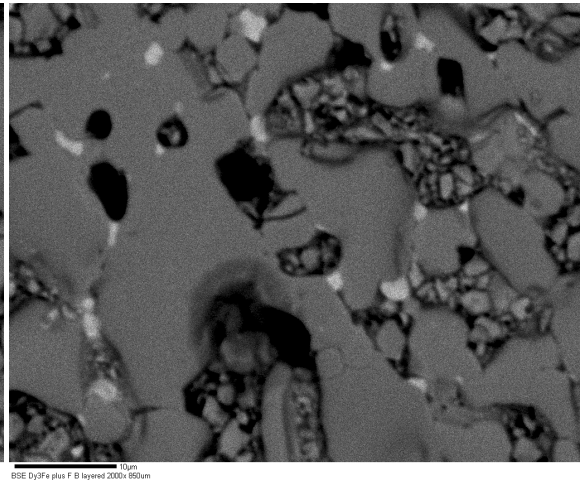
(a)



(b)



(c)



(d)

Figure 3.11 SEM images in BSE mode of $\text{Nd}_2\text{Fe}_{14}\text{B}$ layer in $\text{Nd}_{2.7}\text{Fe}_{14}\text{B}_{1.4}$ /30% $\text{Dy}_{2.34}\text{Fe}$ plus 1.5 Mole Fe_{14}B per mole of Nd liquid mixing powder / $\text{Nd}_{2.7}\text{Fe}_{14}\text{B}_{1.4}$ pellet. At position away from interface 100 μm (a), 350 μm (b), 550 μm (c), and 850 μm (d).

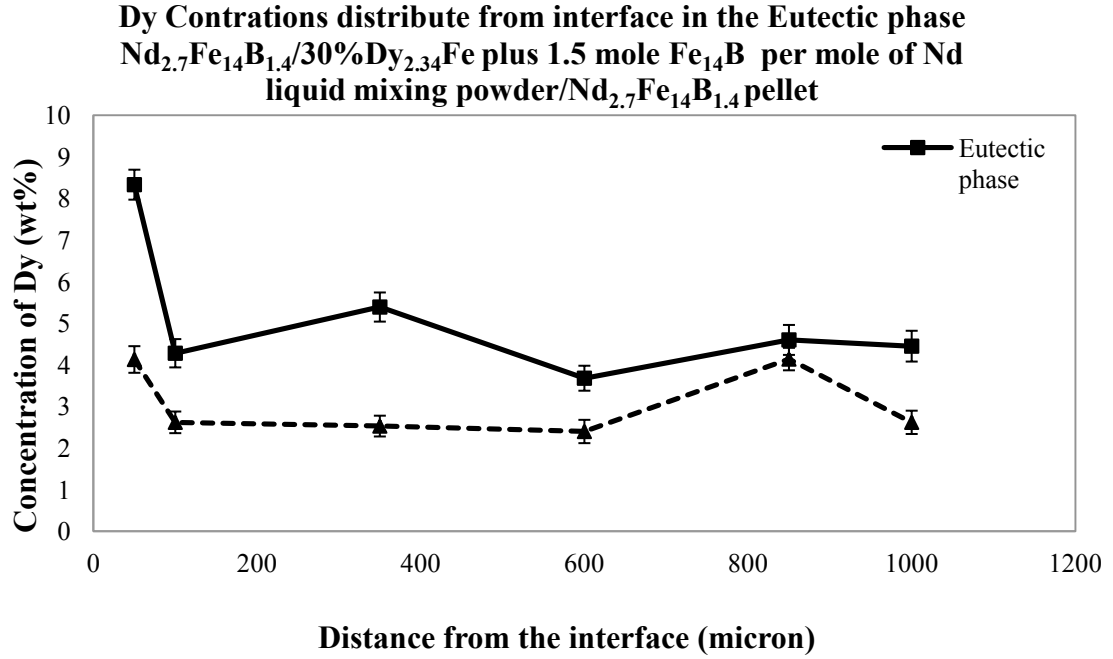


Figure 3.12 The concentration of Dy in eutectic and gray phases of $\text{Nd}_{2.7}\text{Fe}_{14}\text{B}_{1.4}/30\%\text{Dy}_{2.34}\text{Fe}$ plus 1.5 Mole Fe_{14}B per mole of Nd liquid mixing powder/ $\text{Nd}_{2.7}\text{Fe}_{14}\text{B}_{1.4}$ pellet at each distance from the center layer

3.1.4.3 $\text{Nd}_{2.7}\text{Fe}_{14}\text{B}_{1.4}/\text{Dy}_2\text{Fe}_{14}\text{B}$ plus 2at% B/ $\text{Nd}_{2.7}\text{Fe}_{14}\text{B}_{1.4}$ pellet

The microstructure of $\text{Dy}_2\text{Fe}_{14}\text{B}$ plus 2at% B at the center of the layered pellet is displayed in the Figure 3.13. The composition at area A with high Dy composes of 47.67 ± 0.32 wt%Fe, 19.58 ± 0.27 wt%Nd, and 32.74 ± 0.73 wt%Dy. Area B is the Nd rich phase with 31.26 ± 0.25 wt%Fe, 55.84 ± 0.54 wt%Nd, and 12.89 ± 0.55 wt%Dy. Area C is the ferromagnetic phase $\text{Nd}_2\text{Fe}_{14}\text{B}$ that composed of 76.82 ± 0.37 wt%Fe, 7.49 ± 0.16 wt%Nd, and 15.69 ± 0.41 wt%Dy.

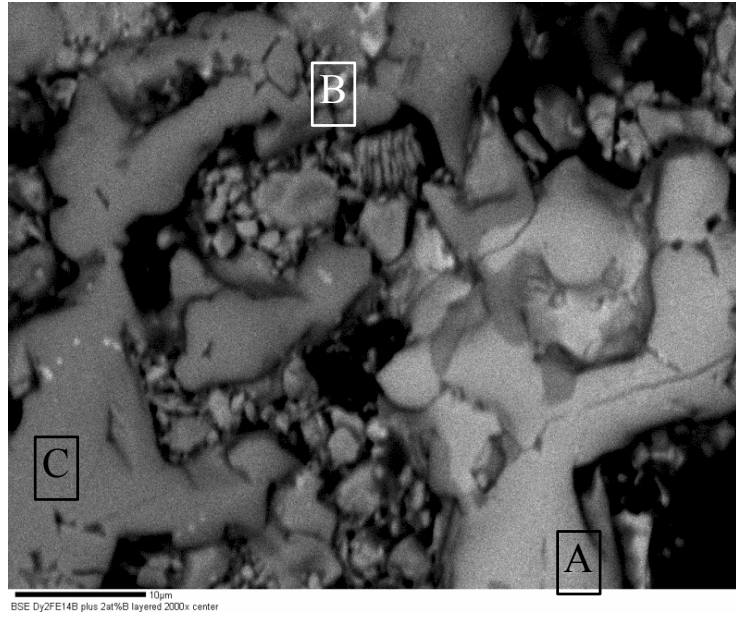
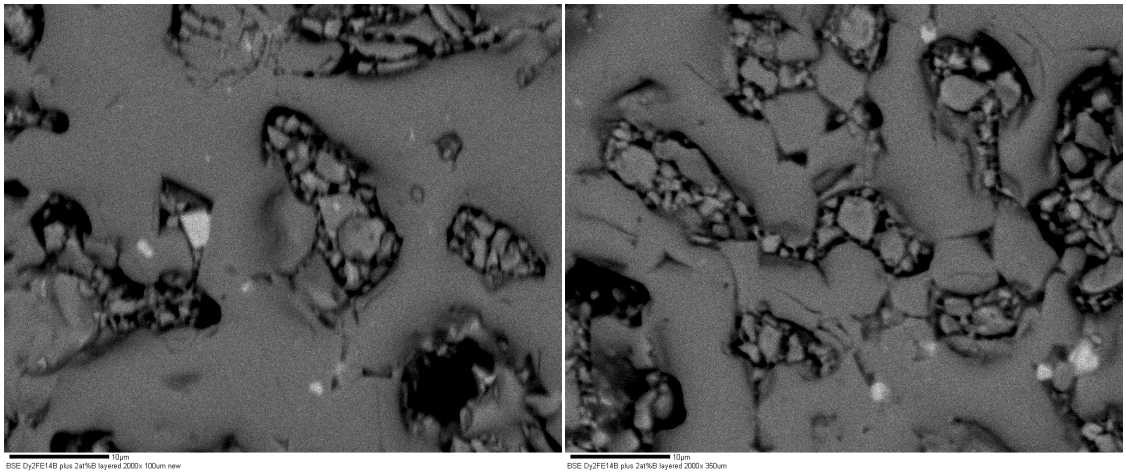


Figure 3.13 Backscattered image of $\text{Dy}_2\text{Fe}_{14}\text{B}$ plus 2at% B at the center layer

The SEM images in Figure 3.14 (a), (b), (c), and (d) show the microstructure in the $\text{Nd}_2\text{Fe}_{14}\text{B}$ layer with the Nd rich phase and $\text{Nd}_2\text{Fe}_{14}\text{B}$ gray phase. The concentration of Dy away from the center layer is presented in Figure 3.15.



(a)

(b)

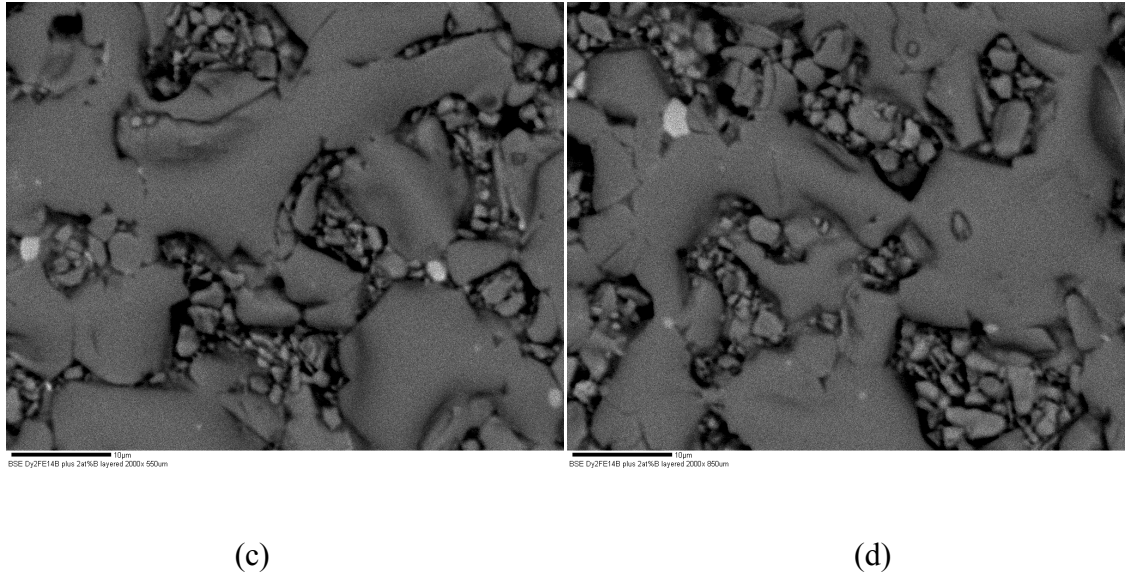


Figure 3.14 SEM images in BSE mode of $\text{Nd}_2\text{Fe}_{14}\text{B}$ layer in $\text{Nd}_{2.7}\text{Fe}_{14}\text{B}_{1.4} / \text{Dy}_2\text{Fe}_{14}\text{B}$ plus 2at% B/ $\text{Nd}_{2.7}\text{Fe}_{14}\text{B}_{1.4}$ pellet. At position away from interface 100 μm (a), 350 μm (b), 550 μm (c), and 850 μm (d).

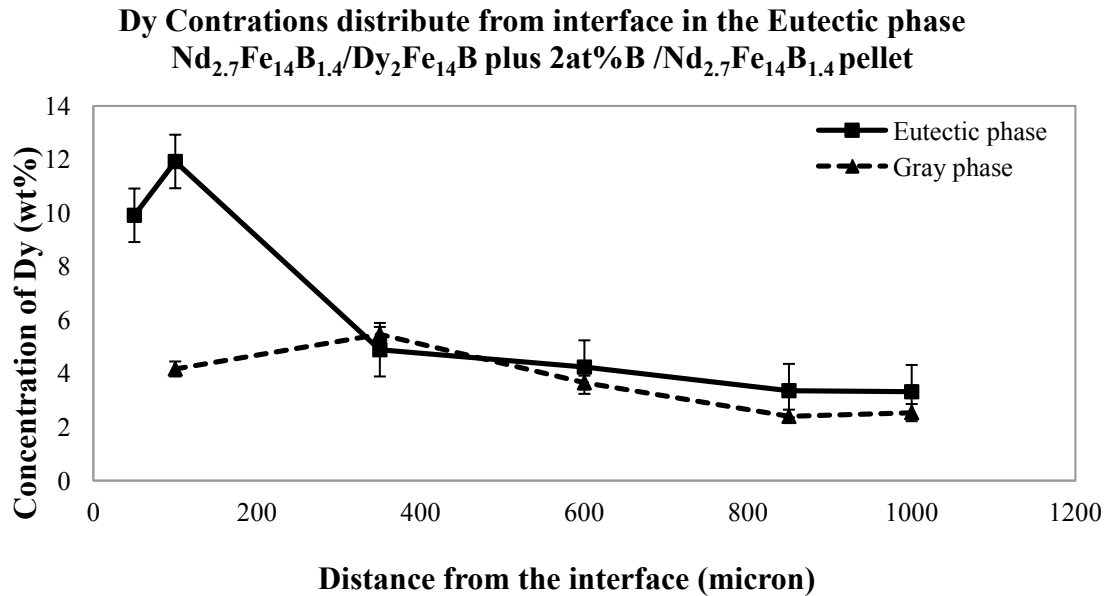


Figure 3.15 The concentration of Dy in eutectic and gray phases of $\text{Nd}_{2.7}\text{Fe}_{14}\text{B}_{1.4} / \text{Dy}_2\text{Fe}_{14}\text{B}$ plus 2at% B/ $\text{Nd}_{2.7}\text{Fe}_{14}\text{B}_{1.4}$ pellet at each distance from the center layer

3.2 The Eutectic liquid and the solid reaction study

3.2.1 Diffusion of Dy in $\text{Nd}_{2.7}\text{Fe}_{14}\text{B}_{1.4}$ composition (Nd rich liquid diffuses into $\text{Dy}_2\text{Fe}_{14}\text{B}$ grain)

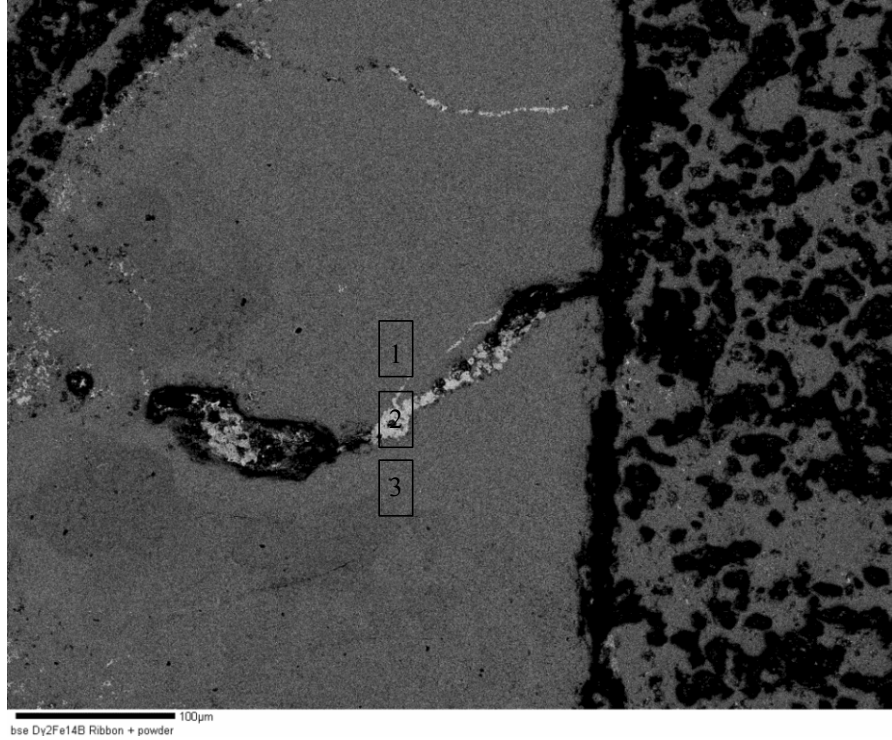
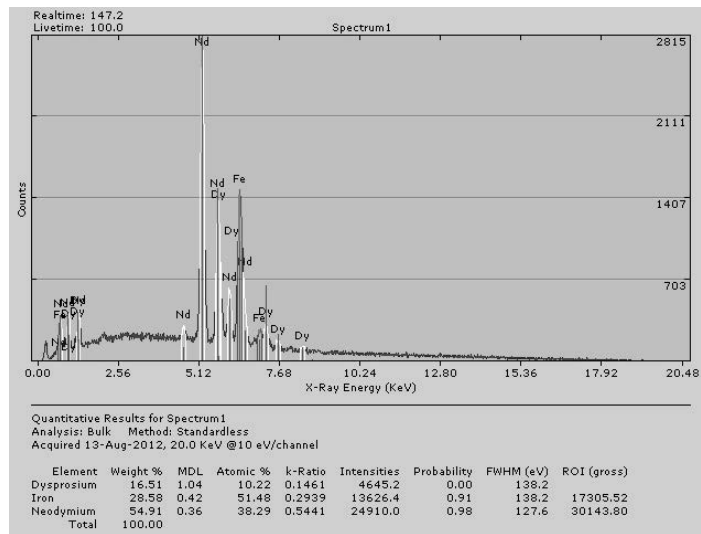


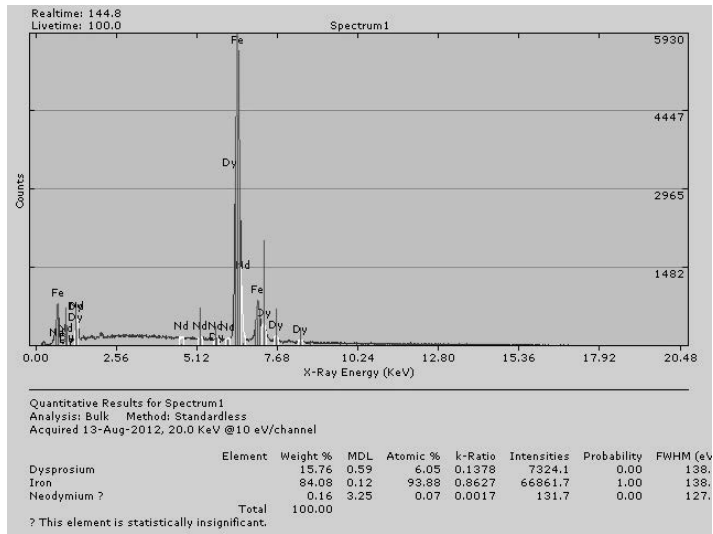
Figure 3.16 BSE image of Nd rich liquid penetrating into Dy ribbon.

An experiment was carried out to examine the interaction of Nd rich eutectic liquid with $\text{Dy}_2\text{Fe}_{14}\text{B}$. $\text{Nd}_{2.7}\text{Fe}_{14}\text{B}_{1.4}$ powder was mixed with pieces of melt spun ribbon with composition $\text{Dy}_2\text{Fe}_{14}\text{B}$. A green pellet of the mixture was produced using cold press under a pressure of 422 MPa. The pellet was sintered under vacuum at 1050°C for 5 hours. Using backscattered electrons to examine the microstructure reveals that Nd liquid has penetrated into the $\text{Dy}_2\text{Fe}_{14}\text{B}$ ribbon (Figure 3.16). The semi-quantitative EDS

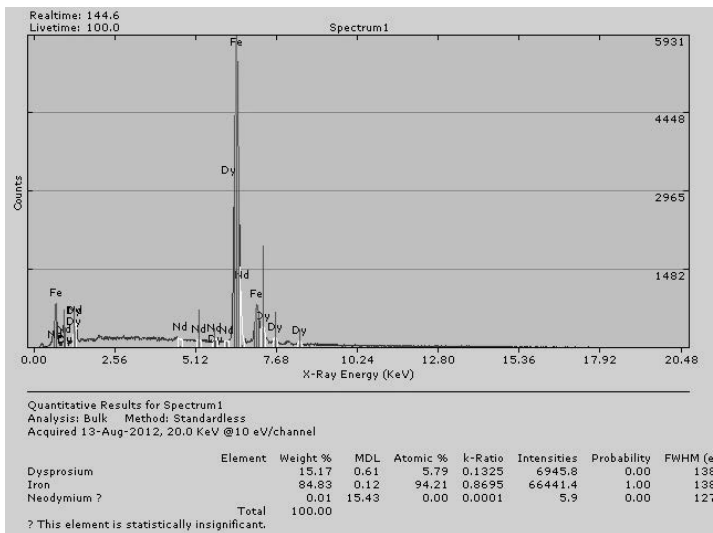
(Figure 3.17) at point 2 shows the Nd rich liquid has dissolved some Dy from the $\text{Dy}_2\text{Fe}_{14}\text{B}$ plate while the surrounding $\text{Dy}_2\text{Fe}_{14}\text{B}$ phase has no detectable Nd. The highest volume fraction of the Nd rich eutectic liquid in the image is found in the $\text{Dy}_2\text{Fe}_{14}\text{B}$ plate, suggesting the Nd rich liquid phase has been drawn into the $\text{Dy}_2\text{Fe}_{14}\text{B}$ plate from $\text{Nd}_{2.7}\text{Fe}_{14}\text{B}_{1.4}$ powder.



(a) Nd rich liquid drawn into the $\text{Dy}_2\text{Fe}_{14}\text{B}$ plate



(b) $\text{Dy}_2\text{Fe}_{14}\text{B}$ plate adjacent to Nd rich liquid



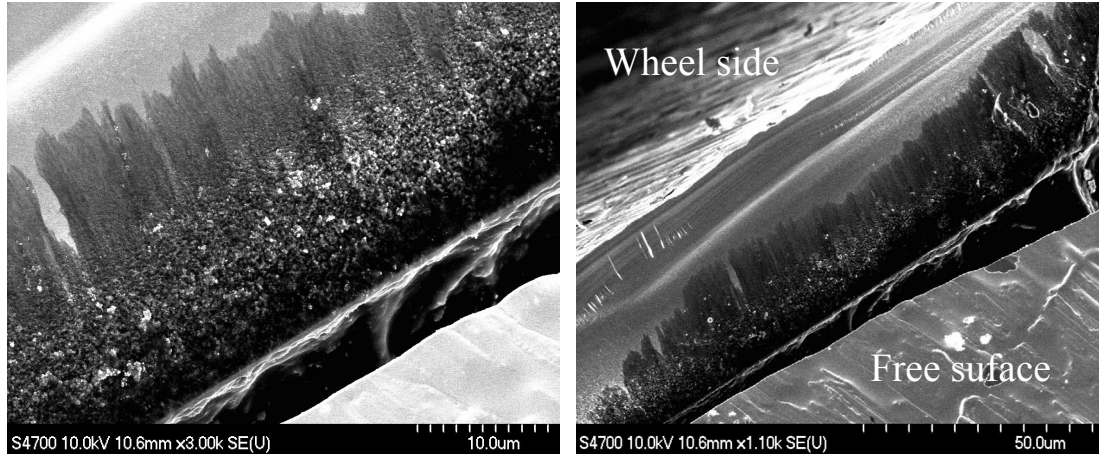
(c) $\text{Dy}_2\text{Fe}_{14}\text{B}$ plate adjacent to Nd rich liquid

Figure 3.17 The standardless EDS results of Dy ribbon that attacked by Nd eutectic liquid. (a) area 1 (b) area 2 (c) area 3

3.2.2 Nd_{2.7}Fe₁₄B_{1.4} ribbons morphology

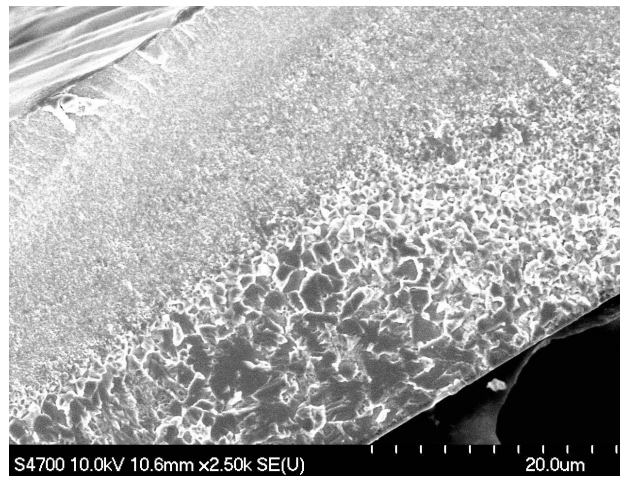
The FE-SEM results in Figure 3.18 show the columnar and equiaxed grains structure of Nd_{2.7}Fe₁₄B_{1.4} melt spun ribbons.

However, the non-uniform sub- μm grain sizes are distinguished. The coarse grains zone is observed in the area that closed to the free surface. The irresolvable structure that is assumed as an amorphous is occurred on the cooling surface that contacted with the wheel. The fine and uniform columnar grains can be found with the distance to the wheel side surface increases as shown in Figure 3.18 (b). It is known that the cooling rate of the melt spinning process is very fast and makes high temperature gradient in the ribbons when they are contacted with the wheel. The formation of the columnar grain structure is also related to the solidification rate and temperature gradient. The small equiaxed grain structure appears close to the cooling surface or the wheel side that have higher solidification rate then the small grain can be formed [36].



(a)

(b)



(c)

Figure 3.18 The cross section micrograph of $\text{Nd}_{2.7}\text{Fe}_{14}\text{B}_{1.4}$ melt spun ribbons.

3.2.3 $\text{Dy}_{2.34}\text{Fe}$ coated $\text{Nd}_{2.7}\text{Fe}_{14}\text{B}_{1.4}$ ribbons before heat treatment

The $\text{Dy}_2\text{Fe}_{14}\text{B}$ ribbon/ $\text{Nd}_{2.7}\text{Fe}_{14}\text{B}_{1.4}$ powder experiment in the previous section suggests a strong interaction between the Nd rich eutectic liquid and the $\text{Dy}_2\text{Fe}_{14}\text{B}$ solid phase. In order to check for the symmetry of this interaction, an experiment was devised

to coat the wheel side of the $\text{Nd}_{2.7}\text{Fe}_{14}\text{B}_{1.4}$ melt spun ribbons with a Dy rich phase via PVD. The Dy vapor source used was $\text{Dy}_{2.34}\text{Fe}$, which is close to the Dy:Fe eutectic composition (Figure 3.2) with eutectic temperature of 878°C . Heating of these coated ribbons above the Dy_3Fe eutectic temperature would allow liquid phase from both $\text{Nd}_{2.7}\text{Fe}_{14}\text{B}_{1.4}$ and $\text{Dy}_{2.34}\text{Fe}$ to contribute to the equilibration process. Heating below 878°C would allow only the $\text{Nd}_{2.7}\text{Fe}_{14}\text{B}_{1.4}$ to contribute to the equilibration process. FESEM analysis was carried out on a fractured cross section of the coated ribbon. Thickness of the deposited layer on the ribbon surface after PVD process was submicron thickness ($\sim 0.3\text{ }\mu\text{m}$) (Figure 3.19). The appearance of two layers in the deposit correlates to the procedure of using two separate coats. The EDS spectrum (Figure 3.20) confirmed that the deposited layer is Dy-Fe composition.

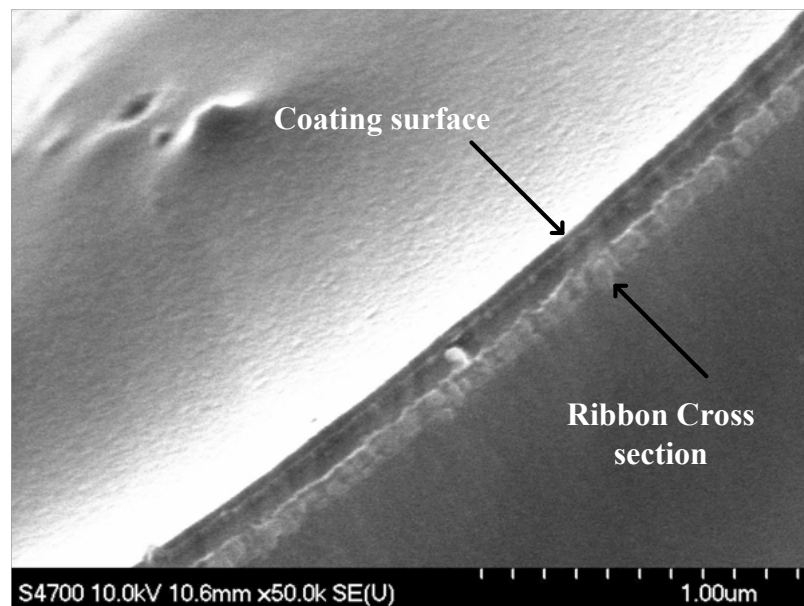


Figure 3.19 FE-SEM image of $\text{Dy}_{2.34}\text{Fe}$ coated $\text{Nd}_{2.7}\text{Fe}_{14}\text{B}_{1.4}$ ribbons before heat treatment

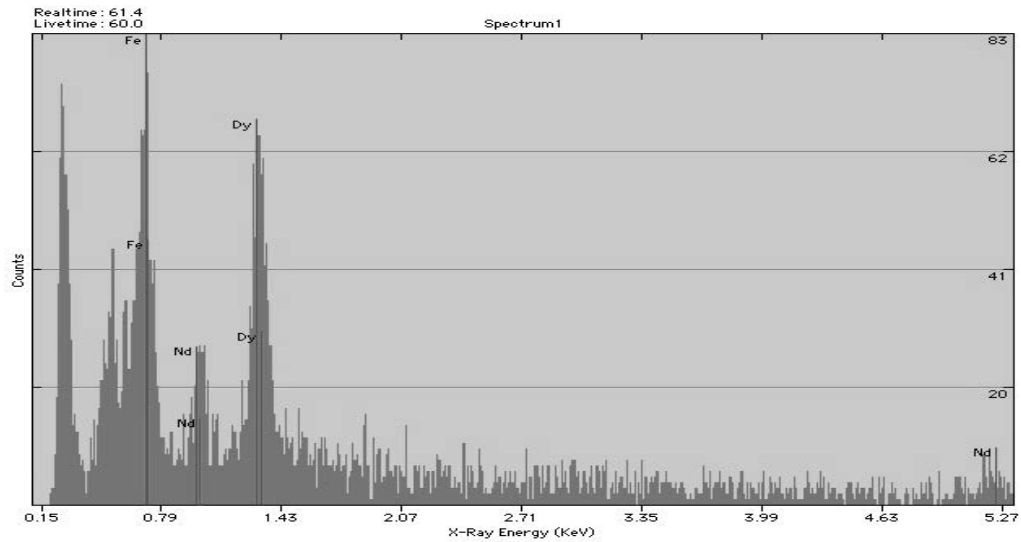


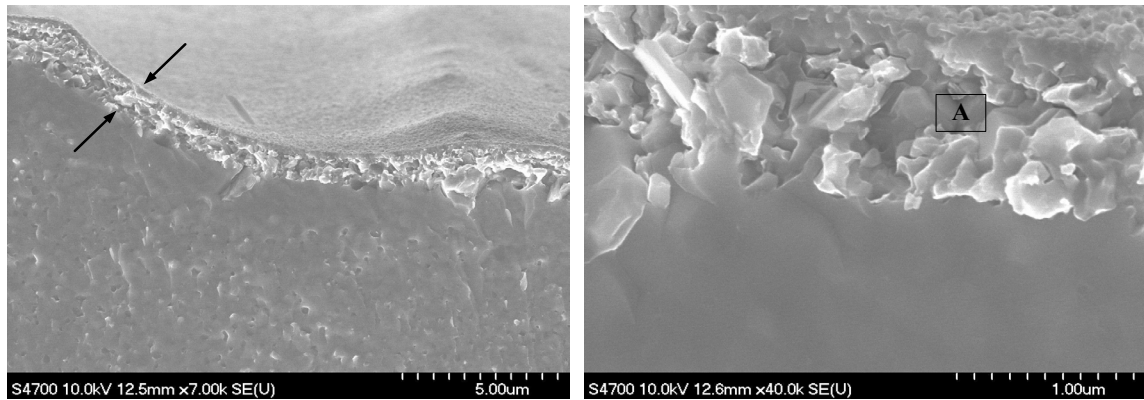
Figure 3.20 EDS spectrum of $\text{Dy}_{2.34}\text{Fe}$ coated $\text{Nd}_{2.7}\text{Fe}_{14}\text{B}_{1.4}$ ribbons before heat treatment

3.2.4 The results of reaction between Nd ribbons and Dy:Fe coating

The influence of thermal treatment was studied to observe the reaction between $\text{Nd}_{2.7}\text{Fe}_{14}\text{B}_{1.4}$ alloy ribbons and $\text{Dy}_{2.34}\text{Fe}$ coating.

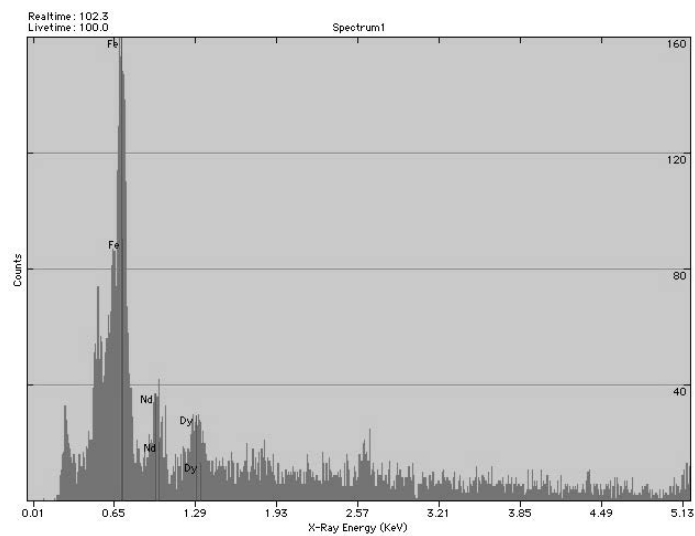
(a) Thermal treatment at 850°C for 1 hour

From the cross section images at 850°C reveals approximately one μm of the $\text{Nd}_{2.7}\text{Fe}_{14}\text{B}_{1.4}/\text{Dy}_{2.34}\text{Fe}$ reaction layer as indicated by the arrow in Figure 3.21(a) and (b). The Fe, Nd and Dy peaks from a standardless EDS spectrum (Figure 3.21(c)) is clearly evident that some of Dy move toward into the $\text{Nd}_{2.7}\text{Fe}_{14}\text{B}_{1.4}$ ribbons during the thermal treatment process.



(a)

(b)



(c)

Figure 3.21 (a,b) FE-SEM images the cross section of thermal treated ribbon at 850°C
(c) EDS spectrum from the reaction area A in figure (b)

Figure 3.22, the fracture surface shows there is no ductile component to structure.
Any rare earth rich metallic phase from the eutectic liquid solidification is seen to be

ductile in fracture cross section magnet materials. This suggests no (or no detectable) liquid phase occurs during thermal treatment process at 850°C.

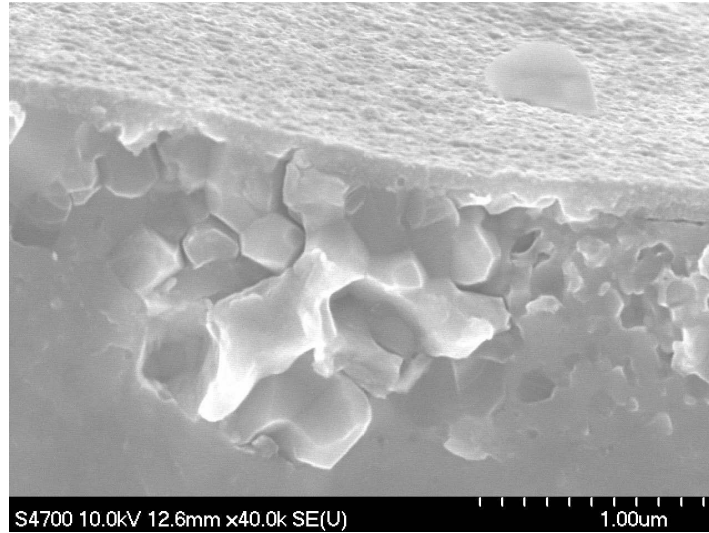


Figure 3.22 FE-SEM image of the cross section of the thermal treated ribbon at 850°C for 1 hour

(b) Thermal treatment at 950°C for 1 hour

The FE-SEM images of the reaction between $\text{Dy}_{2.34}\text{Fe}$ and $\text{Nd}_{2.4}\text{Fe}_{14}\text{B}_{1.4}$ at 950°C are shown in figure 3.23 (a) and (b). The crystallization zone where Dy has penetrated the ribbon of $\text{Nd}_{2.4}\text{Fe}_{14}\text{B}_{1.4}$ is about 3 μm as compared to a crystallization zone of 1 μm thickness at 850°C. The ductile phase along the intergranular or grain boundaries fracture can be seen from Figure 3.24 (a) and (b). The ductile phase is associated with the eutectic liquid transformation to rare earth solid solution during solidification (Figure 3.1 (a, b)). The EDS standardless analysis shows the qualitative and quantitative analysis in area A,

B, and C in figure 3.25. The composition in area A is 79.55 wt% Fe and 20.45 wt% Nd and 0 wt% Dy. Area B is 0.36 wt% Dy, 82.69 wt% Fe and 16.93 wt% Nd. Area C is 6.14 wt% Dy 76.56 wt% Fe, and 17.30 wt% Nd. There is a noticeable feature in area B of a smooth layer $\sim 2\text{ }\mu\text{m}$ thick beneath the crystallization zone. This layer has a small EDS Dy signal. However, the major feature associated with this smooth layer is seen in Figure 3.25, where the ductile ligaments of Nd rich eutectic phase can be seen below the smooth layer but not in the smooth layer. This may be an indication that the Nd liquid has been drawn into the reaction zone by a chemical driving force associated with the negative energy of mixing for Nd:Dy in the liquid and the solid phases.

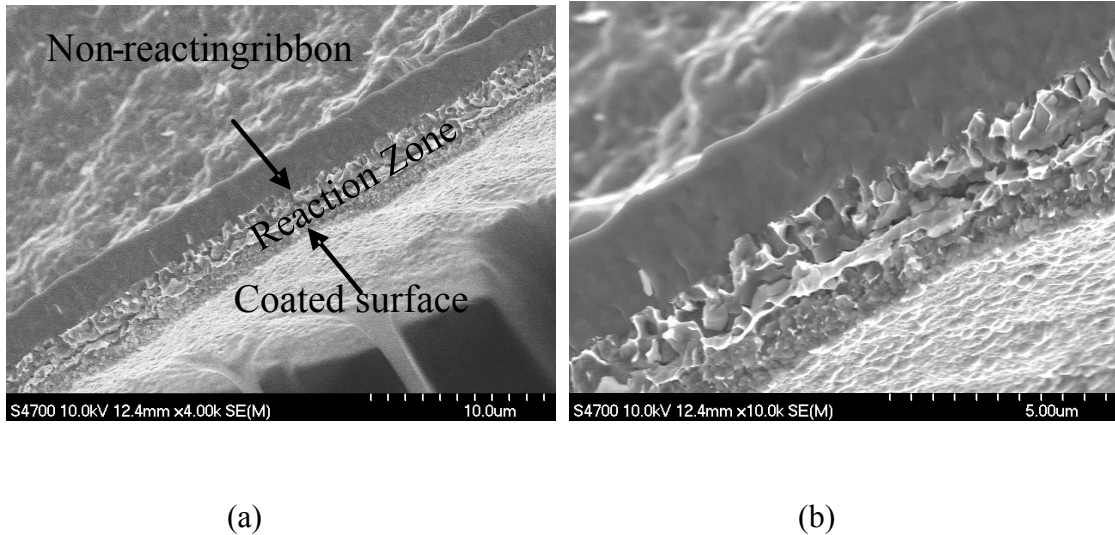


Figure 3.23 (a,b) FE-SEM images the cross section of thermal treated ribbon at 950°C

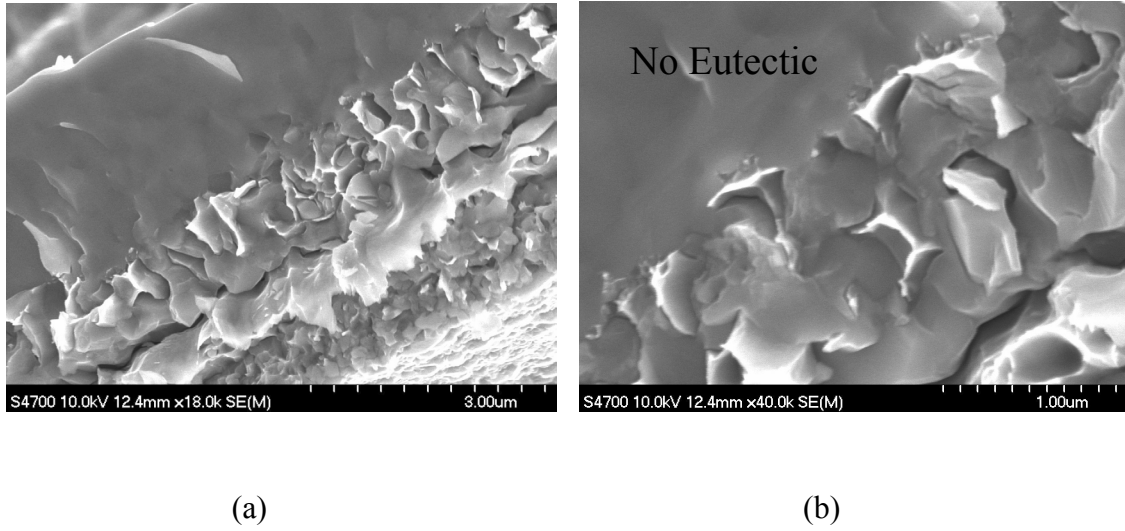


Figure 3.24 (a,b) FE-SEM images the cross section of thermal treated ribbon at 950°C

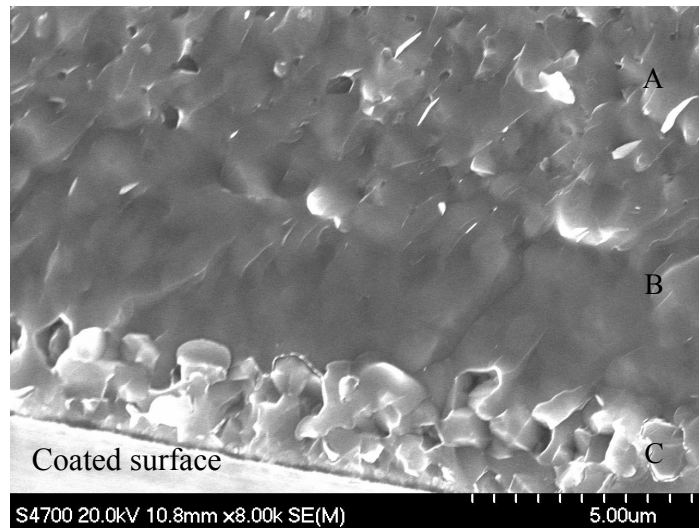


Figure 3.25 FE-SEM image of the cross section of thermal treated ribbon at 950°C

The well-known phenomenon of dissolution:precipitation for grain coarsening has been applied to Nd rich liquid: $\text{Nd}_2\text{Fe}_{14}\text{B}$ liquid phase sintering [37, 38]. During the thermal treatment process at 950°C, both the $\text{Dy}_{2.34}\text{Fe}$ (878°C eutectic temperature) and

the $\text{Nd}_{2.4}\text{Fe}_{14}\text{B}_{1.4}$ are melted. Especially, the fine $\text{Nd}_{2.4}\text{Fe}_{14}\text{B}_{1.4}$ particles and their sharp edge of large particles are dissolved into the melted $\text{Dy}_{2.34}\text{Fe}$ [37]. Figure 3.26 illustrates the mechanism during heat treatment process. At the higher temperature than eutectic temperature of $\text{Dy}_{2.34}\text{Fe}$, the Dy liquid eutectic phase occurs and mixes with Nd liquid from dissolved $\text{Nd}_{2.4}\text{Fe}_{14}\text{B}_{1.4}$ grains. The mixing of Nd-Dy liquid eutectic phase is reprecipitated, forming relatively large $(\text{Nd,Dy})_2\text{Fe}_{14}\text{B}$ particles. This mechanism is called dissolution:reprecipitation process [37].

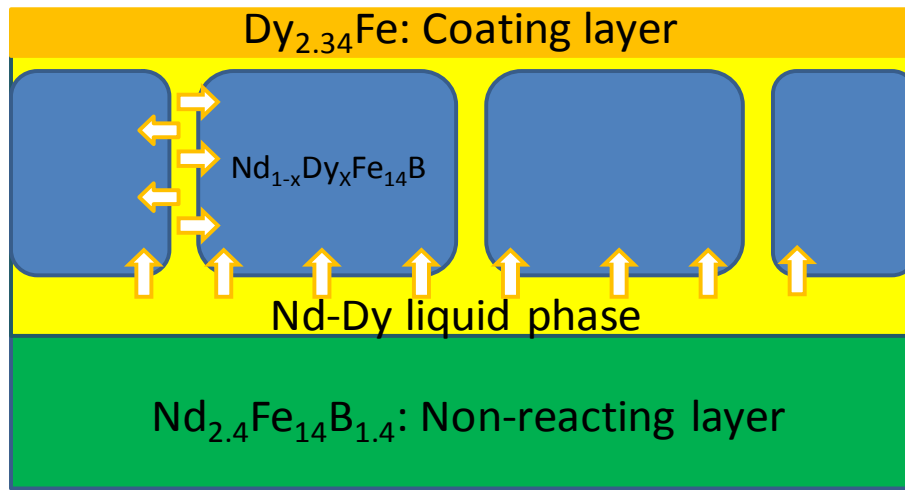


Figure 3.26 The schematic illustrates mechanism during thermal treatment process.

The solid state diffusion of Dy in $\text{Nd}_2\text{Fe}_{14}\text{B}$ has been recently studied. "Diffusion coefficients for Dy, Nd and Fe into $\text{Nd}_2\text{Fe}_{14}\text{B}$ are given according an Arrhenius equation $D=D_0 \exp (-Q/RT)$. For Dy diffusion into $\text{Nd}_2\text{Fe}_{14}\text{B}$, $Q=315 \text{ kJ/mol}$ and $D_0=8 \cdot 10^{-4} \text{ m}^2/\text{s}$. [25]" We can compare the reaction zone width to the volume diffusion length as a method to see if dissolution:precipitation is occurring in this experiment. Using the idea

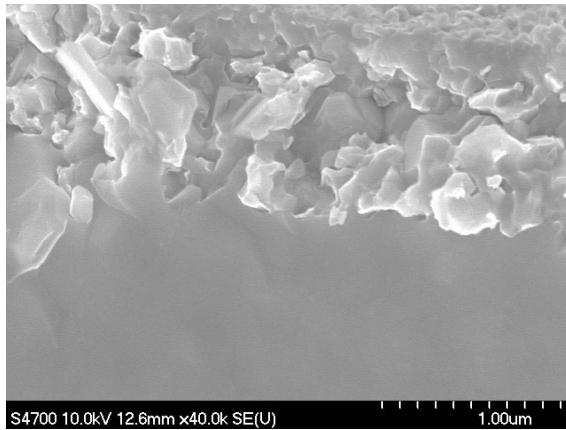
that the reaction layer thickness is $2\sqrt{Dt}$, we can compare the effective diffusion coefficient to the volume diffusion coefficient. This is done in Table 3.1. It can be seen that the effective diffusion coefficient observed is 1 to 3 orders of magnitude lower than the volume diffusion coefficient. This indicates that a mechanism other than volume diffusion is responsible for the width of the reaction zone. Given the observations in figure 3.16 and the observations in this section, it is proposed that a dissolution:precipitation process is contributing to the Dy homogenization process.

Table 3.1 Diffusion coefficient and effective diffusion length of Dy_{2.34}Fe coated Nd_{2.4}Fe₁₄B_{1.4} ribbon.

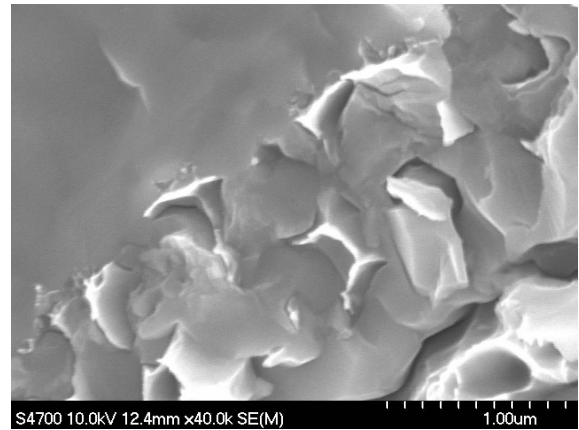
Sample geometry	Temperature (°C)	Diffusion coefficient (cm ² /s)	Effective diffusion length
Dy _{2.34} Fe coated Nd _{2.4} Fe ₁₄ B _{1.4} Ribbon: Reaction layer (1 µm) Including non-reacting layer (5 µm)	850	6.94x10 ⁻¹³ 1.74x10 ⁻¹¹	1x10 ⁻⁴ 5x10 ⁻⁴
Dy _{2.34} Fe coated Nd _{2.4} Fe ₁₄ B _{1.4} Ribbon: Reaction layer (3 µm) Including non-reacting layer (5 µm)	950	6.25x10 ⁻¹² 1.74x10 ⁻¹¹	3x10 ⁻⁴ 5x10 ⁻⁴
Dy Volume Diffusion into Nd ₂ Fe ₁₄ B grains (Reference [35])	850 950	1.78x10 ⁻¹⁴ 2.81x10 ⁻¹³	1.60x10 ⁻⁵ 6.36x10 ⁻⁵

Figure 3.27 demonstrates the FE-SEM images of the reacted layer between Dy_{2.34}Fe and Nd_{2.4}Fe₁₄B at 850°C (a) and 950°C (b) together. The reacted particles' grain

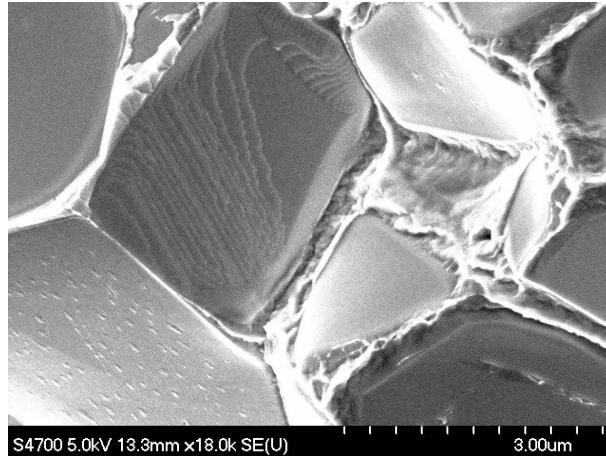
size at 850°C is lesser than the grain size of particles that heat treatment at 950°C. The average grain size of the coated ribbons at 850°C is approximately 200 nanometers compare with 300 to 500 nanometers for the coated ribbons that heat-treated at 950°C. This is because of at higher temperature; the Dy-Nd liquid can be diffused into $\text{Nd}_2\text{Fe}_{14}\text{B}$ grains and moved the boundary of the grains to the outward direction. This results in the greater of the grains or grain coarsening in order to reduce the total energy due to the total grain boundary areas decrease during sintering process [39]. As from the dissolution-re-precipitation mechanism, only the large $(\text{Nd,Dy})\text{Fe}_{14}\text{B}$ grains can be observed at 950°C which shrinkage and disappear of fine particles[37].



(a)



(b)



(c)

Figure 3.27 FE-SEM images of the fracture surface of thermal treated ribbon at (a) 850°C and (b) 950°C. (c) Sintered $\text{Nd}_{2.7}\text{Fe}_{14}\text{B}_{1.4}$ fracture surface showing ductile Nd rich phase at the grain boundary.

The motion of Nd rich liquid into $\text{Dy}_2\text{Fe}_{14}\text{B}$ (Figure 3.16) and the motion of Dy rich liquid into $\text{Nd}_{2.7}\text{Fe}_{14}\text{B}_{1.4}$ ribbon (Figure 3.25) is proposed to be correlated with the dissolution of the solid phase into the liquid. Liquid motion is driven by pressure gradients in the liquid. Although gradients in capillary forces in a powder pack can be a driving force for liquid, a term relating solid dissolution to liquid motion is also considered. In a closed thermodynamic system, a change of internal energy (U) can be related to the heat transfer (Q) and work (W) in the system. The internal energy in a reversible process can be expressed by combining the first and second laws of thermodynamic by assuming that the mass or volume of liquid phase does not change and atoms in liquid never change and stay constant.

The First law of Thermodynamics,

The work done on the system is related to pressure (P) and volume (V) associates with the addition of the component powder (N_i) in the system and its chemical potential (μ).

$$dU = \partial Q - PdV + \sum_i \mu_i dN_i \quad (3.3)$$

The Second law of thermodynamic,

The heat transfer is associated with temperature (T) and entropy (S)

$$\partial Q = TdS \quad (3.4)$$

Therefore, the change in internal energy becomes

$$dU = TdS - PdV + \sum_i \mu_i dN_i \quad (3.5)$$

The Euler equation is

$$U = TS - PV + \sum_i \mu_i N_i \quad (3.6)$$

The first differential of The Euler equation according the rule of calculus

$$dU = TdS + SdT - PdV + VdP + \sum_i \mu_i dN_i + N_i d\mu_i \quad (3.7)$$

Since dU in equation 3.5 is equal to dU in equation 3.7, then

$$0 = TdS - PdV + \sum_i d\mu_i N_i \quad (3.8)$$

Which leads to the Gibbs-Duhem equation as

$$\sum_{i=1}^i N_i d\mu_i = -SdT + VdP \quad (3.9)$$

According to the Gibbs-Duhem equation, the chemical potential change and the amount of Nd and Dy particles can be correlated to the changing of pressure. For this to be an isothermal, spontaneous process

$$\sum_{i=1}^i X_i d\mu_i = \Omega dP < 0 \quad (3.10)$$

Where we have divided through by the number of atoms per unit volume, giving the maximum decrease in pressure due to the dissolution process. Fluid flow occurs in response to a gradient in pressure. For example, the average velocity of laminar flow in a pipe is given by the Hagen–Poiseuille equation as

$$Velocity_{average} = \frac{Radius^2}{8 * Viscosity} \frac{dp}{d(position)} \quad (3.11)$$

Differentiating equation 3.3 and 3.6 with position (y) leads to

$$\sum_{i=1}^i X_i \frac{d\mu_i}{dy} = \Omega \frac{dP}{dy} \quad (3.12)$$

To attempt a derivation of the effect, we consider the solid and liquid are ideal solutions.

Then using the Darken trick

$$X_i d\mu_i = X_i d(\mu_o + kT \ln(X_i)) = X_i \left[\frac{1}{X_i} d(X_i) \right] \quad (3.13)$$

We can write for the Dy and Nd atoms 'changing places' between the solid and liquid, with Fe and B remaining the same configuration and a partition coefficient of 1.

$$dX_{Dy} = (C_{DySolid} - C_{DyLiquid}) \frac{\Omega}{2} \quad (3.14)$$

$$dX_{Nd} = ([\Omega^{-1} - C_{DyLiquid}] - [\Omega^{-1} - C_{NdSolid}]) \frac{\Omega}{2} \quad (3.15)$$

$$\sum_i X_i d\mu_i = kT((C_{DySolid} - C_{DyEut})\Omega) \quad (3.16)$$

This means that the Hagen–Poiseuille equation can have the form

$$V = Constant * \frac{d}{dy} (C_{DySolid} - C_{DyEut}) \quad (3.17)$$

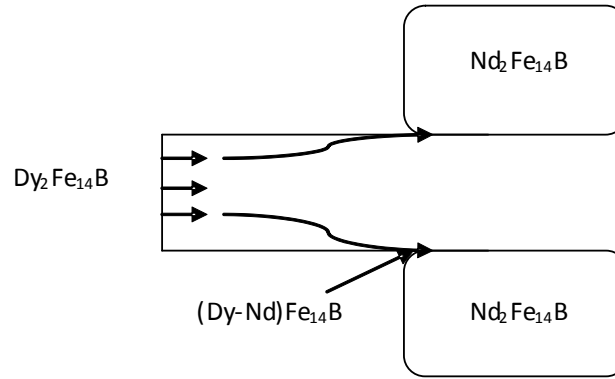


Figure 3.28 Illustration of the proposed solution/precipitation process

In Figure 3.21 shows the proposed solution/precipitation process, with Dy atoms in the solid moving into the Nd rich liquid as the solid Dy source dissolves. The Dy atoms leave the liquid with the Nd atoms to precipitate out an (Nd,Dy)₂Fe₁₄B alloy in equilibrium with the liquid. The dissolution of the solid causes the liquid to displace.

The $\text{Dy}_{2.34}\text{Fe}$ that has eutectic temperature lower than the heat treatment temperature is melted and transforms to liquid phase during the solidification process. The fluid flow from big porosity in the center of layered into small pores next to the interface can be described by the capillary force mechanism. The smaller pore size sucks the Dy liquid in the middle layered throughout the porosity in $\text{Nd}_{2.7}\text{Fe}_{14}\text{B}_{1.4}$ powder pack.

The Dy concentration changing with time in the eutectic and solid phases are determined by Fick's second law and the flux atoms moving from solid to liquid. The diffusion coefficient of Dy in liquid phase (D), liquid velocity into pore (V) and the reaction between liquid and solid (h) were considered. The correlation of these parameters due to the Dy diffusion in liquid Nd rich or eutectic phase, in $\text{Nd}_2\text{Fe}_{14}\text{B}$ or solid phase, and the correlation of h with the grain boundary area are obtained by equation (3.16), (3.17), and (3.18) respectively [40]. Starting with the definition of flux, J with a velocity component

$$J = -D \cdot \left(\frac{d}{dy} C_{DyEut} \right) + V(y) \cdot C_{Eut} \quad (3.16)$$

Then taking into account a possible dissolution:precipitation reaction between the liquid and the solid using a transport coefficient, h , controlling the rate at which the liquid and solid are equilibrated.

$$\frac{d}{dt} C_{Eut} = -\frac{d}{dy} J - h \cdot (C_{Eut} - C_{solid}) = D \frac{d^2}{dy^2} C_{Eut} - \left(\frac{d}{dy} V(y) C_{Eut} \right) - V(y) \cdot \left(\frac{d}{dy} C_{Eut} \right) - h \cdot (C_{Eut} - C_{solid}) \quad (3.17)$$

Where the rate of change of the composition of the solid at each y is correlated with the difference in the solid and liquid concentrations (partition coefficient = 1)

$$\frac{d}{dt}C_{Solid} = h \cdot (C_{Eut} - C_{Solid}) \quad (3.18)$$

$$h = D \times (Grain\ boundary\ area) \quad (3.19)$$

Where C_{DyEut} is Dy concentration in eutectic or Nd-rich phase (atoms/cm³)

$C_{DySolid}$ is Dy concentration in solid or Nd_{2.7}Fe₁₄B_{1.4} grain (atoms/cm³)

D is diffusion coefficient of Dy (cm²/s)

V is velocity of Dy

t is diffusion time (s)

x is diffusion length (cm)

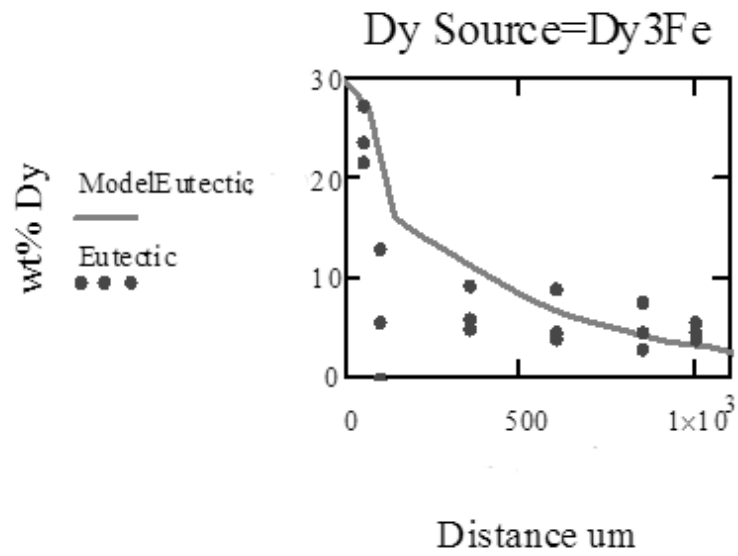
h is the transport coefficient for the dissolution:precipitation reaction between liquid and solid (1/s)

The Dy concentration boundary condition at the interface between the Dy source layer and the pellet was allowed to be time dependent.

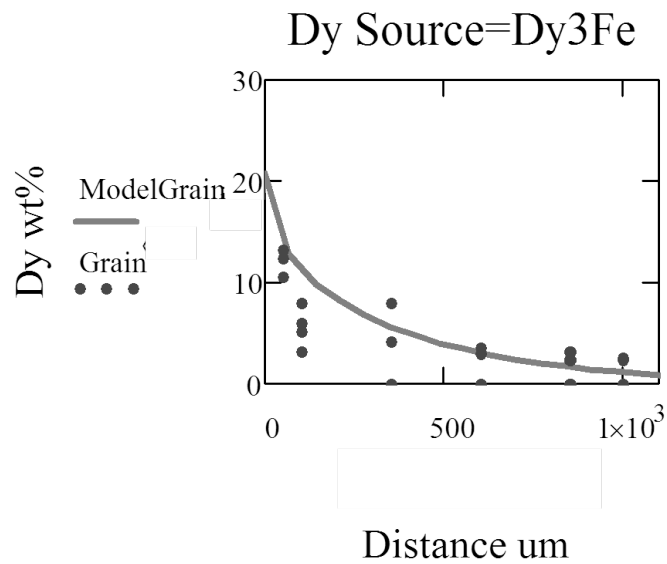
$$\frac{dC_{Eutectic\ Boundary}}{dt} = J_{Boundary} \left(\frac{1}{length} \right) \quad (3.20)$$

The length refers to the thickness of the Dy source layer that can provide Dy to the pellet multiplied by the ratio of available liquid in the layer to liquid in the pellet.

This model is fit to the concentration profile of Dy determined experimentally for the grain and eutectic phases. The fit parameters are the constant in equation 3.17, the liquid phase diffusion coefficient, D , in equation 3.16, the transfer coefficient h in equation 3.17, and the length in equation 3.20. The comparison of the model fit with the experimental data is shown in figures 3.29, 3.30, and 3.31. It is seen that the gradient in Dy composition is reduced in the from $\text{Dy}_2\text{Fe}_{14}\text{B}$ plus 2at%B and $\text{Dy}_{2.34}\text{Fe}$ plus Fe_{14}B sources compared to $\text{Dy}_{2.34}\text{Fe}$. The model fit parameters are shown in Table 3.2. The liquid velocity, diffusion coefficient and transfer coefficient are all of similar value. The length term related to the availability of liquid in the Dy source layer in the boundary condition equation 3.20 is the term with the greatest variation. This indicates the reduced gradient observed from the $\text{Dy}_2\text{Fe}_{14}\text{B}$ plus 2at%B and $\text{Dy}_{2.34}\text{Fe}$ plus Fe_{14}B sources is related to the rapid Dy sources depletion. The value of h is significant, suggesting that the dissolution:precipitation process is active in the Dy transport process. The alternative mechanism for increasing the Dy content in the solid is solid state diffusion, which is seen to be of very small magnitude at 950°C as described in Table 3.4.

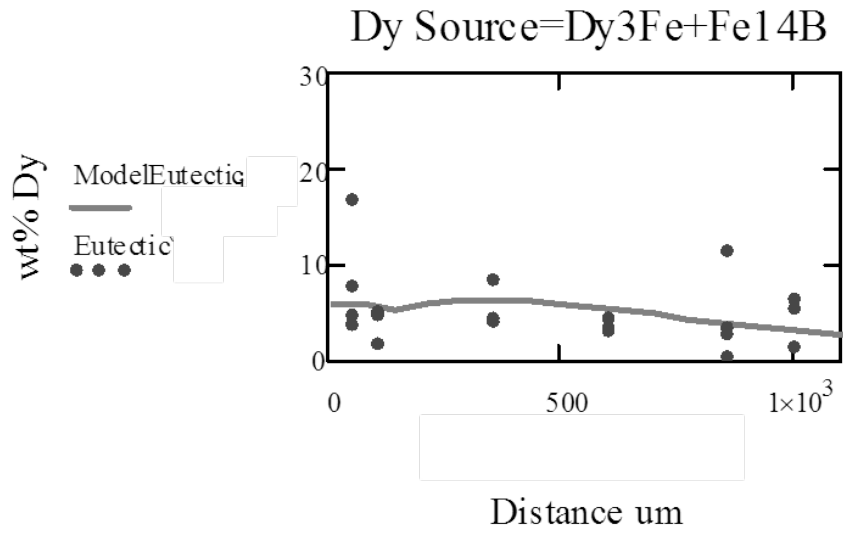


(a)

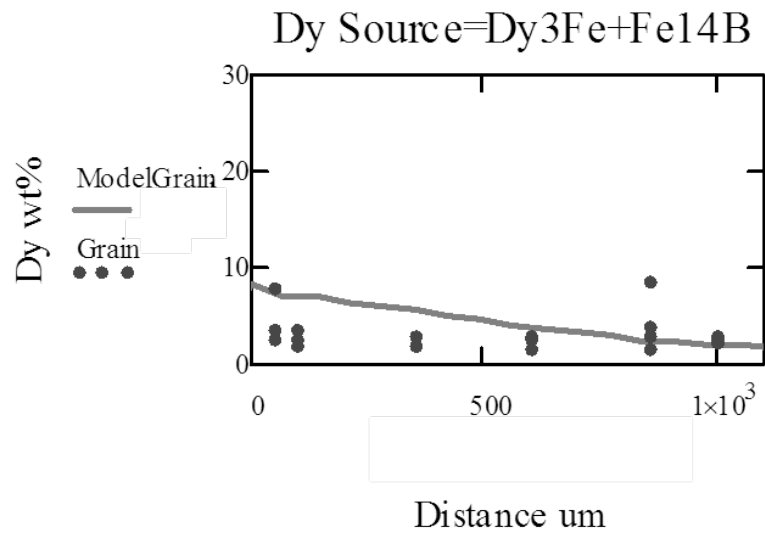


(b)

Figure 3.29 Concentration profile of Dy vary with depth from the interface for Dy_{2.34}Fe as Dy source (a) Dy concentration in eutectic phase (b) Dy concentration in the grain

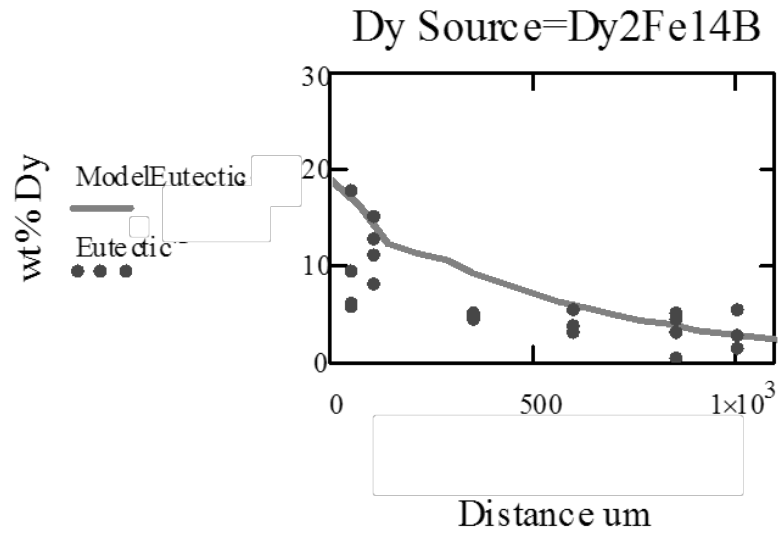


(a)

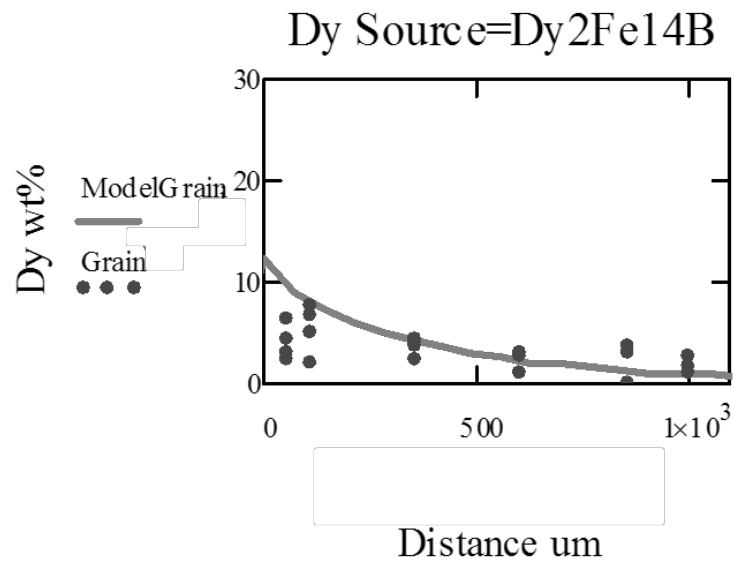


(b)

Figure 3.30 Concentration profile of Dy vary with depth from the interface for Dy_{2.34}Fe plus Fe₁₄B as Dy source (a) Dy concentration in eutectic phase (b) Dy concentration in the grain



(a)



(b)

Figure 3.31 Concentration profile of Dy vary with depth from the interface for Dy₂Fe₁₄B plus 2at%B as Dy source (a) Dy concentration in eutectic phase (b) Dy concentration in the grain

Table 3.2 The diffusion coefficient, velocity, and reaction between liquid and solid parameters

Sample geometry	Diffusion coefficient (cm²/s)	Velocity (cm/s)	h (1/s)	d (μm)
Layered pellet: Dy _{2.34} Fe	3x10 ⁻⁷	1.6x10 ⁻⁷	1.25x10 ⁻⁴	40
Layered pellet: Dy ₂ Fe ₁₄ B + 2at%B	2.45x10 ⁻⁷	4.88x10 ⁻⁷	1.10x10 ⁻⁴	8
Layered pellet: Dy _{2.34} Fe + Fe ₁₄ B	2.45x10 ⁻⁷	1.2x10 ⁻⁷	1.10x10 ⁻⁴	17

In porous materials, the diffusion coefficient of a liquid phase is modulated by the pore fraction, ϵ , and tortuosity, τ .

$$D_{porous} = \frac{D^* \epsilon}{\tau} \quad (3.21)$$

The pore fraction and the tortuosity in some materials are shown in Table 3.3. Base on the totruisity of these material, the τ value is about 1 to 10. In our experiment, the fraction of the Nd rich liquid phase in pores is about 3% that corresponded to ϵ approximately 0.03. Thus, the diffusion coefficients of Dy in Nd_{2.7}Fe₁₄B_{1.4} powder packs from our experiments are lower than other elements in other systems.

Table 3.3 Porosity and tortuosity factors in catalyst materials [41]

Catalyst Material	Pore fraction, ϵ	Tortuosity, τ
100–110 μm powder packed into a tube	0.416	1.56
pelletized Cr_2O_3 supported on Al_2O_3	0.22	2.5
pelletized boehmite alumina	0.34	2.7
Girdler G-58 Pd on alumina	0.39	2.8
Haldor-Topsøe MeOH synthesis catalyst	0.43	3.3
0.5% Pd on alumina	0.59	3.9
1.0% Pd on alumina	0.5	7.5
pelletized Ag/8.5% Ca alloy	0.3	6
pelletized Ag	0.3	10

3.3 The comparison of the effective diffusion length

The diffusion coefficient of Dy in coated $\text{Nd}_{2.4}\text{Fe}_{14}\text{B}_{1.4}$ ribbons with $\text{Dy}_{2.34}\text{Fe}$ are calculated from equation 3.22

$$2\sqrt{Dt} = \text{Thickness of reaction layer of ribbon} \quad (3.22)$$

The effective diffusion length is calculated by a following equation

$$\sqrt{(2\sqrt{Dt})^2 + (Vt)^2} = \text{Effective diffusion length} \quad (3.23)$$

The results from the calculations of Dy diffusion coefficient and their effective diffusion length are shown in Table 3.4. The Dy diffusion coefficient in the heat-treated ribbons at 950°C is greater than the heat treated ribbons at 850°C because of the higher temperature, the more atoms can diffuse. This leads to the higher effective diffusion length in 950°C heat-treated ribbons. The diffusion coefficient and the effective diffusion length of the layered pellets are very much higher than in the coated ribbons because there is no porosity in the coated ribbons.

Table 3.4 The diffusion coefficient and effective diffusion length of layered pellets and coated $\text{Nd}_{2.4}\text{Fe}_{14}\text{B}_{1.4}$ ribbons

Sample geometry	Temperature (°C)	Diffusion coefficient (cm^2/s)	Effective diffusion length
Layered pellet: $\text{Dy}_{2.34}\text{Fe}$	950	3×10^{-7}	1.46×10^{-1}
Layered pellet: $\text{Dy}_2\text{Fe}_{14}\text{B} + 2\text{at}\%\text{B}$		2.45×10^{-7}	1.33×10^{-1}
Layered pellet: $\text{Dy}_{2.34}\text{Fe} + \text{Fe}_{14}\text{B}$		2.45×10^{-7}	1.33×10^{-1}
$\text{Dy}_{2.34}\text{Fe}$ coated $\text{Nd}_{2.4}\text{Fe}_{14}\text{B}_{1.4}$ Ribbon: Reaction layer (1 μm)	850	6.94×10^{-13}	1×10^{-4}
Including non-reacting layer (5 μm)		1.74×10^{-11}	5×10^{-4}
$\text{Dy}_{2.34}\text{Fe}$ coated $\text{Nd}_{2.4}\text{Fe}_{14}\text{B}_{1.4}$ Ribbon: Reaction layer (3 μm)	950	6.25×10^{-12}	3×10^{-4}
Including non-reacting layer (5 μm)		1.74×10^{-11}	5×10^{-4}
Dy diffuse into $\text{Nd}_2\text{Fe}_{14}\text{B}$ grains	850	1.78×10^{-14}	1.60×10^{-5}
	950	2.81×10^{-13}	6.36×10^{-5}

The diffusion coefficient of Dy in $\text{Nd}_2\text{Fe}_{14}\text{B}$ grain at temperature 850°C and 950°C are calculated by using the equation and parameters from Compos's studied [25].

$$D = D_0 \exp(-Q/RT) \quad (3.24)$$

Where Q is 315 kJ/mol, D_0 is $8 \times 10^{-4} \text{ m}^2/\text{s}$, and R is gas constant 8.314 J/mol.K.

Conclusions

1. The study of eutectic liquid and the solid reaction reveals that the Nd rich liquid phase or eutectic liquid is drawn into $\text{Dy}_2\text{Fe}_{14}\text{B}$ grain. The diffusion of Dy in $\text{Nd}_{2.7}\text{Fe}_{14}\text{B}_{1.4}$ composition results indicate that the reaction of dissolution/reprecipitation process between $\text{Dy}_{2.34}\text{Fe}$ and $\text{Nd}_{2.7}\text{Fe}_{14}\text{B}_{1.4}$ ribbons causes the recrystallization in the reaction zone with significant presence of eutectic phase at 950°C , but not at 850°C . This correlates to the eutectic temperature of $\text{Dy}_{2.34}\text{Fe}$ at 878°C .
2. A model including the proposed driving force for liquid phase flow can simulate aspects of the experimental data of composition of the eutectic and solid phases with as a function of depth from the surface. The effective diffusion coefficients of Dy in $\text{Nd}_{2.7}\text{Fe}_{14}\text{B}_{1.4}$ powder pack at 950°C were calculated based on the fit of experiment data from EDS results with the model. The diffusion coefficient of Dy for $\text{Dy}_{2.34}\text{Fe}$, $\text{Dy}_2\text{Fe}_{14}\text{B}$ plus 2at%B, and $\text{Dy}_{2.34}\text{Fe}$ plus Fe_{14}B in the layered pellets are $3 \times 10^{-7} \text{ cm}^2/\text{s}$, $2.45 \times 10^{-7} \text{ cm}^2/\text{s}$, and $2.45 \times 10^{-7} \text{ cm}^2/\text{s}$, respectively. The diffusion coefficient of Dy for $\text{Dy}_{2.34}\text{Fe}$ in $\text{Nd}_{2.7}\text{Fe}_{14}\text{B}_{1.4}$ ribbons is $6.25 \times 10^{-12} \text{ cm}^2/\text{s}$. Result for the effective diffusion length of Dy for $\text{Dy}_{2.34}\text{Fe}$ in $\text{Nd}_{2.7}\text{Fe}_{14}\text{B}_{1.4}$ layered pellets as $1.46 \times 10^{-1} \text{ cm}$ is higher than the effective diffusion length in $\text{Nd}_{2.7}\text{Fe}_{14}\text{B}_{1.4}$ ribbons as $3 \times 10^{-4} \text{ cm}$ because there is no porosity in the ribbons.

3. The simulation:experimental data comparison suggests that the use of $\text{Dy}_2\text{Fe}_{14}\text{B}$ plus 2at%B, and $\text{Dy}_{2.34}\text{Fe}$ plus Fe_{14}B as Dy source results in a rapid depletion of Dy at the layer/pellet interface as compared to the $\text{Dy}_{2.34}\text{Fe}$ source. This is interpreted as a method to control the efficiency of Dy transport through control of Dy rich liquid availability. The higher melting point of $\text{Dy}_2\text{Fe}_{14}\text{B}+2\text{at}\%\text{B}$ than $\text{Dy}_{2.34}\text{Fe}$ can limit the supply of Dy in the eutectic liquid phase as compared to $\text{Dy}_{2.34}\text{Fe}$. The excess of Fe and B in $\text{Dy}_{2.34}\text{Fe}+\text{Fe}_{14}\text{B}$ compound can interact with Nd or Dy in the eutectic liquid phase, again reducing availability of the liquid phase.

References

- [1] S. Sugimoto, "Current status and recent topics of rare-earth permanent magnets," *Journal of Physics D-Applied Physics*, vol. 44, Feb 16 2011.
- [2] M.-H. Y. Choi, Ji-Hun ; Kim, Dong-Hwan ; Kim, In-Bae ; Kim, Yang-Do "Coercivity enhancement in Nd₂Fe₁₄B permanent magnetic powders through rotating diffusion process with DyH_x powders," *Journal of Magnetism*, vol. 116, pp. 342-349, 2011.
- [3] X. B. Liu and Z. Altounian, "The partitioning of Dy and Tb in NdFeB magnets: A first-principles study," *Journal of Applied Physics*, vol. 111, Apr 1 2012.
- [4] R. S. L. L.Q. Yu, K.T. Dong, and Y.P. Zhang. (2012). *Key techniques for ultrahigh performance sintered Nd-Fe-B magnets preparation*.
- [5] C. T. S. Tsai D.S., Hsu S.E., Hung M.P., Fe-Nd-B phase diagram [Online]. Available: <http://www1.asminternational.org/AsmEnterprise/APD>
- [6] S. H. Masato Sagawa, Hitoshi Yamamoto, Setsuo Fujimura and Yutaka Matsuura, "Nd–Fe–B permanent magnet materials," *Japanese Journal of Applied Physics* vol. 26, pp. 785-800, 1987.
- [7] H. Fukunaga, I. Yamamoto, M. Nakano, and T. Yanai, "Magnetic properties of Dy-diffused Nd-Fe-B powder prepared by crystallization from amorphous state," *Journal of Applied Physics*, vol. 111, Apr 1 2012.
- [8] M. Choi, D. Kim, J. Yu, and Y. Kim, "Improvement of the magnetic properties of Nd₂Fe₁₄B powders by dysprosium diffusion," *Reviews on Advanced Materials Science*, vol. 28, pp. 134-140, Jul 2011.
- [9] K. H. J. B. C. H. de Groot, and F. R. de Boer, "Two-powder Nd₂Fe₁₄B magnets with DyGa addition," *J. Appl. Phys.*, vol. 83, pp. 388-393, January 1998.
- [10] S. F. Masato Sagawa, Hitoshi Yamamoto, and Yutaka Matsuura, "Permanent magnet materials based on the Rare Earth-Iron-Boron tetragonal compounds," *IEEE Transactions on Magnetism*, vol. 20, pp. 1584-1589, 1984.
- [11] J. B. H. Gordon B. Haxel, and Greta J. Orris. (2002, November 20, 2002). *Rare earth elements—critical resources for high technology*. Available: <http://pubs.usgs.gov/fs/2002/fs087-02/>
- [12] D. Brown, B. M. Ma, and Z. M. Chen, "Developments in the processing and properties of NdFeB-type permanent magnets," *Journal of Magnetism and Magnetic Materials*, vol. 248, pp. 432-440, Aug 2002.
- [13] M. Soderznik, K. Z. Rozman, S. Kobe, and P. McGuinness, "The grain-boundary diffusion process in Nd-Fe-B sintered magnets based on the electrophoretic deposition of DyF₃," *Intermetallics*, vol. 23, pp. 158-162, Apr 2012.
- [14] H. M. Koshi Yoshimura, Tomoori Odaka, "R-Fe-B type rare earth sintered magnet and process for production of the same," United States Patent US8206516B2, 2012.
- [15] H. M. Koshi Yoshimura, Tomoori Odaka, "R-Fe-B type rare earth sintered magnet and the process for production the same," United States Patent US8187392B2, 2012.

- [16] H. Sepehri-Amin, T. Ohkubo, and K. Hono, "Grain boundary structure and chemistry of Dy-diffusion processed Nd-Fe-B sintered magnets," *Journal of Applied Physics*, vol. 107, p. 09A745, 2010.
- [17] H. Fukunaga, Y. Sugimoto, M. Nakano, T. Yanai, S. Ohta, M. Itakura, and M. Nishida, "Coercivity enhancement of Dy-coated Nd-Fe-B flakes by crystallization," *Journal of Applied Physics*, vol. 109, Apr 1 2011.
- [18] F. Xu, J. Wang, X. P. Dong, L. T. Zhang, and J. S. Wu, "Grain boundary microstructure in DyF₃-diffusion processed Nd-Fe-B sintered magnets," *Journal of Alloys and Compounds*, vol. 509, pp. 7909-7914, Jul 28 2011.
- [19] S. H. Tomoki Fukagawa, "Coercivity generation of surface Nd₂Fe₁₄B grains and mechanism of fcc-phase formation at the Nd/Nd₂Fe₁₄B interface in Nd-sputtered Nd-Fe-B sintered magnets," *JOURNAL OF APPLIED PHYSICS* vol. 104, 2008.
- [20] H. Suzuki, Y. Satsu, and M. Komuro, "Magnetic properties of a Nd-Fe-B sintered magnet with Dy segregation," *Journal of Applied Physics*, vol. 105, pp. 07A734-3, 2009.
- [21] M. I. Natsuki Watanabe, Noriyuki Kuwano, Deshan Li, Shunji Suzuki, and Ken-ich Machida, "Microstructure Analysis of Sintered Nd-Fe-B Magnets Improved by Tb-Vapor Sorption," *Materials Transactions*, vol. 48, pp. 915-918, 2007.
- [22] K. Hirota, H. Nakamura, T. Minowa, and M. Honshima, "Coercivity enhancement by the grain boundary diffusion process to Nd-Fe-B sintered magnets," *Magnetism, IEEE Transactions on*, vol. 42, pp. 2909-2911, 2006.
- [23] S. S. Deshan Li, Takashi Kawasaki, and Ken-ichi Machida, "Grain interface modification and magnetic properties of Nd-Fe-B sintered magnets," *Japanese Journal of Applied Physics*, vol. 47, pp. 7876-7878, 2008.
- [24] (2013, 2/10). *New alloying process by grain boundary diffusion*. Available: <http://www.shinetsu-rare-earth-magnet.jp/e/rd/grain.html>.
- [25] M. F. de Campos, "Diffusion coefficients of interest for the simulation of heat treatment in rare-earth transition metal magnets," in *Materials Science Forum*, 2012, pp. 163-168.
- [26] T. Fujita, Z. Horita, and T. G. Langdon, "Using grain boundary engineering to evaluate the diffusion characteristics in ultrafine-grained Al-Mg and Al-Zn alloys," *Materials Science and Engineering: A*, vol. 371, pp. 241-250, 2004.
- [27] E. M. M. Robert J. Twiss, *Structural Geology*.
- [28] W. F. Li, H. Sepehri-Amin, T. Ohkubo, N. Hase, and K. Hono, "Distribution of Dy in high-coercivity (Nd,Dy)-Fe-B sintered magnet," *Acta Materialia*, vol. 59, pp. 3061-3069, 2011.
- [29] J. Fidler and T. Schrefl, "Overview of Nd-Fe-B magnets and coercivity," *Journal of Applied Physics*, vol. 79, pp. 5029-5034, 1996.
- [30] Available: http://en.wikipedia.org/wiki/Mass_diffusivity
- [31] K. E. E. David A. Porter, *Phase Transformations in Metals and Alloys*, 2nd ed.: Chapman&Hall, 1992.
- [32] B. G. E. Nourtier-Mazauric, B. Fritz, E. Brosse, D. Garcia and A. Clément, "Modelling the Dissolution/Precipitation of Ideal Solid Solutions," *Oil & Gas Science and Technology Rev. IFP*, vol. 60 pp. 401-415, 2005.

- [33] I. Barin, *Thermochemical data of pure substances*. Weinheim, Federal Republic of Germany; New York: VCH, 1993.
- [34] O. H. Dy-Fe phase diagram [Online]. Available:
<http://www1.asminternational.org/AsmEnterprise/APD>
- [35] H. E. T. Grieb B., Schneider G., and Petzow G. B-Dy-Fe phase diagram [Online]. Available: <http://www1.asminternational.org/AsmEnterprise/AP>
- [36] X. Jing, Y. Shihong, Y. Dunbo, L. Zongan, L. Shipeng, and L. Hongwei, "Influence of solidification rate on microstructures of cast strips and corresponding sintered NdFeB magnets," *Journal of Rare Earths*, vol. 24, pp. 306-309, 2006.
- [37] L. Xianglian and Z. Shouzeng, "Grain growth behavior in sintered Nd-Fe-B magnets," *Journal of Rare Earths*, vol. 25, pp. 329-335, 2007.
- [38] F. Vial, F. Joly, E. Nevalainen, M. Sagawa, K. Hiraga, and K. Park, "Improvement of coercivity of sintered NdFeB permanent magnets by heat treatment," *Journal of Magnetism and Magnetic Materials*, vol. 242, pp. 1329-1334, 2002.
- [39] W. D. Callister and D. G. Rethwisch, *Fundamentals of materials science and engineering : an integrated approach*. Hoboken, NJ: John Wiley & Sons, 2008.
- [40] S. A. Hackney, "Unpublished."
- [41] (2011, 2/10/13). Available:
<http://jbrwww.che.wisc.edu/home/jbraw/chemreacfun/ch7/slides-masswrxn-2up.pdf>

Appendix A: The composition of eutectic and solid phases in Nd₂Fe₁₄B layer away from the center layer of the Nd_{2.7}Fe₁₄B_{1.4}/30%Dy_{2.34}Fe/Nd_{2.7}Fe₁₄B_{1.4} pellet

Table A.1 The composition of Nd rich phase (Eutectic phase) in Nd₂Fe₁₄B layer of the Nd_{2.7}Fe₁₄B_{1.4}/30%Dy_{2.34}Fe/Nd_{2.7}Fe₁₄B_{1.4} pellet

Distance from the interface	Eutectic phase		
	Fe K-family	Nd L-family	Dy M-family
50 micron	29.94±0.25	48.39±0.48	21.67±0.55
	29.33±0.26	46.43±0.48	23.64±0.59
	18.22±0.21	54.53±0.53	27.25±0.68
Average	25.83±0.24	49.78±0.50	24.19±0.61
100 micron	2.53±0.12	85.45±0.68	13.01±0.38
	19.65±0.19	74.74±0.67	5.61±0.33
	26.50±0.22	73.50±0.67	0±3.84
Average	32.5±0.14	83.96±0.75	12.79±0.42
	20.30±0.17	79.41±0.69	7.85±1.24
350 micron	2.40±0.11	88.44±0.70	9.17±0.33
	7.40±0.14	86.88±0.77	5.73±0.35
	8.45±0.16	86.46±0.78	5.09±0.34
Average	6.08±0.14	87.26±0.75	6.66±0.34
600 micron	2.74±0.12	88.47±0.71	8.80±0.33
	2.91±0.13	93.27±0.82	3.82±0.34
	36.24±0.25	59.13±0.55	4.63±0.31
Average	13.96±0.17	80.29±0.69	5.75±0.33
850 micron	8.10±0.14	87.44±0.70	4.46±0.27
	24.52±0.21	71.14±0.65	4.33±0.32
	5.25±0.13	91.92±0.81	2.83±0.32
Average	11.9±0.17	80.56±0.73	7.53±0.37
	12.44±0.16	82.77±0.72	4.79±0.32
1000 micron	3.79±0.12	90.89±0.72	5.31±0.28
	13.80±0.17	82.24±0.73	3.96±0.33
	18.67±0.19	76.82±0.69	4.50±0.32
Average	12.09±0.16	83.32±0.71	4.59±0.31

Table A.2 The composition of Nd₂Fe₁₄B phase (Gray phase) in Nd₂Fe₁₄B layer of the Nd_{2.7}Fe₁₄B_{1.4}/30%Dy_{2.34}Fe/Nd_{2.7}Fe₁₄B_{1.4} pellet

Distance from the interface	Gray phase		
	Fe K-family	Nd L-family	Dy M-family
50 micron	65.49±0.34	21.29±0.27	13.22±0.40
	71.79±0.35	17.62±0.24	10.59±0.35
	70.21±0.35	17.38±0.23	12.41±0.39
Average	69.16±0.35	18.76±0.25	12.07±0.38
100 micron	73.08±0.31	18.92±0.22	8.0±0.28
	60.86±0.32	33.91±0.36	5.23±0.29
	68.49±0.34	28.36±0.31	3.15±0.26
	72.64±0.35	21.33±0.26	6.03±0.28
Average	68.77±0.33	25.63±0.29	5.60±0.28
350 micron	74.92±0.32	25.08±0.26	0±0.03
	72.33±0.35	19.64±0.25	8.03±0.31
	73.05±0.35	22.84±0.27	4.12±0.25
Average	73.44±0.34	22.52±0.26	4.05±0.20
600 micron	72.87±0.31	23.61±0.25	3.53±0.23
	71.98±0.35	25.08±0.29	2.94±0.27
	74.20±0.36	25.80±0.30	0±4.34
Average	73.01±0.34	24.83±0.28	2.16±1.61
850 micron	72.46±0.31	24.40±0.25	3.14±0.22
	73.78±0.36	26.22±0.30	0±4.29
	73.01±0.35	26.99±0.30	0±4.33
	71.63±0.35	29.92±0.29	2.45±2.24
Average	72.72±0.34	26.88±0.28	1.40±2.77
1000 micron	72.31±0.31	24.99±0.26	2.69±0.22
	69.53±0.35	30.47±0.33	0±4.30
	72.16±0.35	25.34±0.29	2.50±0.26
Average	71.33±0.34	26.93±0.29	1.73±1.59

Appendix B: The composition of eutectic and solid phases in Nd₂Fe₁₄B layer away from the center layer of the Nd_{2.7}Fe₁₄B_{1.4}/30% Dy_{2.34}Fe plus 1.5 mole Fe₁₄B per mole of Nd liquid mixing powder/ Nd_{2.7}Fe₁₄B_{1.4} pellet

Table B.1 The composition of Nd rich phase (Eutectic phase) in Nd₂Fe₁₄B layer of the Nd_{2.7}Fe₁₄B_{1.4}/30% Dy_{2.34}Fe plus 1.5 mole Fe₁₄B per mole of Nd liquid mixing powder/ Nd_{2.7}Fe₁₄B_{1.4} pellet

Distance from the interface	Eutectic phase		
	Fe K-family	Nd L-family	Dy M-family
50 micron	7.48±0.15	87.60±0.78	4.92±0.31
	5.80±0.14	90.28±0.80	3.92±0.33
	25.93±0.25	57.32±0.56	16.75±0.48
	20.75±0.2	71.52±0.65	7.72±0.34
Average	14.99±0.19	76.68±0.70	8.33±0.36
100 micron	30.72±0.24	64.14±0.60	5.14±0.34
	28.94±0.26	69.14±0.67	1.92±0.40
	14.13±0.18	80.58±0.73	5.29±0.35
	20.07±0.19	75.18±0.67	4.75±0.3
Average	23.47±0.22	72.26±0.67	4.28±0.34
350 micron	6.86±0.15	88.69±0.79	4.44±0.31
	7.31±0.15	88.23±0.79	4.47±0.36
	28.57±0.23	67.21±0.62	4.22±0.32
	7.86±0.15	83.71±0.75	8.44±0.4
Average	12.65±0.17	81.96±0.74	5.39±0.35
600 micron	3.36±0.12	93.34±0.82	3.30±0.28
	22.66±0.20	73.02±0.66	4.32±0.30
	35.23±0.24	61.34±0.57	3.43±0.31
Average	20.42±0.19	75.9±0.68	3.68±0.30
850 micron	28.65±0.24	59.73±0.57	11.62±0.51
	35.08±0.25	61.32±0.58	3.59±0.36
	34.08±0.24	62.92±0.58	3±0.28
	6.87±0.14	89.03±0.78	0.41±0.29
Average	26.17±0.22	68.25±0.6275	4.66±0.36
1000 micron	8.03±0.15	85.41±0.76	6.46±0.38
	21.44±0.21	77.06±0.70	1.50±0.33
	3.63±0.13	90.97±0.81	5.40±0.39
Average	11.03±0.16	84.48±0.76	4.45±0.37

Table B.2 The composition of $\text{Nd}_2\text{Fe}_{14}\text{B}$ phase (Gray phase) in $\text{Nd}_{2.7}\text{Fe}_{14}\text{B}_{1.4}$ layer of the $\text{Nd}_{2.7}\text{Fe}_{14}\text{B}_{1.4}/30\% \text{Dy}_{2.34}\text{Fe}$ plus 1.5 Mole Fe_{14}B per mole of Nd liquid mixing powder/
 $\text{Nd}_{2.7}\text{Fe}_{14}\text{B}_{1.4}$ pellet

Distance from the interface	Gray phase		
	Fe K-family	Nd L-family	Dy M-family
50 micron	72.89±0.35	24.56±0.28	2.55±0.27
	72.90±0.35	24.64±0.29	2.45±0.24
	58.63±0.35	33.28±0.38	8.08±0.53
	72.83±0.35	23.72±0.27	3.45±0.24
Average	69.31±0.35	26.55±0.305	4.13±0.32
100 micron	72.77±0.35	25.42±0.29	1.80±0.22
	70.69±0.36	26.84±0.31	2.47±0.29
	71.18±0.35	25.15±0.29	3.67±0.29
	72.78±0.34	24.69±0.28	2.53±0.24
Average	71.86±0.35	25.52±0.29	2.62±0.26
350 micron	72.97±0.35	25.26±0.29	1.77±0.22
	68.71±0.35	28.42±0.32	2.86±0.26
	64.56±0.33	32.65±0.35	2.78±0.27
	72.39±0.35	2.47±0.28	2.71±0.25
Average	69.66±0.34	22.2±0.31	2.53±0.25
600 micron	67.09±0.34	31.29±0.34	1.61±0.28
	57.66±0.32	39.41±0.41	2.93±0.29
	71.93±0.35	25.42±0.29	2.66±0.27
Average	65.56±0.34	32.04±0.35	2.4±0.28
850 micron	72.07±0.34	19.49±0.24	8.44±0.33
	70.14±0.34	26.00±0.30	3.86±0.29
	72.21±0.35	25.00±0.29	2.79±0.25
	73.55±0.35	25.00±0.29	1.45±0.22
Average	71.99±0.34	23.87±0.28	4.14±0.27
1000 micron	71.46±0.36	25.47±0.30	3.07±0.28
	66.48±0.33	30.91±0.33	2.61±0.26
	72.09±0.35	25.72±0.30	2.19±0.30
Average	70.01±0.35	27.37±0.31	2.62±0.28

Appendix C: The composition of eutectic and solid phases in Nd₂Fe₁₄B layer away from the center layer of the Nd_{2.7}Fe₁₄B_{1.4}/Dy₂Fe₁₄B plus 2at% B/Nd_{2.7}Fe₁₄B_{1.4} pellet

Table C.1 The composition of Nd rich phase (Eutectic phase) in Nd_{2.7}Fe₁₄B_{1.4} layer of the Nd_{2.7}Fe₁₄B_{1.4}/Dy₂Fe₁₄B plus 2at% B/Nd_{2.7}Fe₁₄B_{1.4}

Distance from the interface	Eutectic phase		
	Fe K-family	Nd L-family	Dy M-family
50 micron	4.49±0.15	89.30±0.80	6.21±0.31
	5.47±0.15	84.91±0.77	9.61±0.44
	24.16±0.21	69.83±0.64	6.0±0.31
	4.11±0.14	78.07±0.70	17.82±0.51
Average	9.56±0.16	80.53±0.73	9.91±0.39
100 micron	12.57±0.17	79.15±0.71	8.28±0.38
	10.89±0.19	77.90±0.71	11.21±0.38
	15.26±0.20	69.48±0.65	15.26±0.50
	4.05±0.14	83.02±0.74	12.93±0.42
Average	10.69±0.18	77.39±0.70	11.92±0.42
350 micron	15.43±0.19	79.91±0.73	4.67±0.37
	8.31±0.16	87.10±0.79	4.59±0.32
	12.17±0.17	82.59±0.74	5.24±0.33
	23.16±0.20	71.80±0.65	5.04±0.34
Average	14.77±0.18	80.35±0.7275	4.89±0.34
600 micron	15.71±0.19	81.00±0.73	3.29±0.39
	33.87±0.23	62.15±0.57	3.98±0.30
	7.90±0.16	86.65±0.78	5.45±0.40
Average	19.16±0.19	76.6±0.69	4.24±0.36
850 micron	4.73±0.13	90.15±0.79	5.12±0.31
	7.38±0.14	88.01±0.78	4.61±0.35
	26.36±0.21	70.36±0.64	3.28±0.31
	6.87±0.14	89.03±0.78	0.41±0.29
Average	11.34±0.16	84.39±0.75	3.36±0.32
1000 micron	24.34±0.22	72.79±0.67	2.87±0.32
	3.29±0.13	91.09±0.81	5.61±0.37
	28.55±0.23	69.97±0.65	1.48±0.36
Average	18.73±0.19	77.95±0.71	3.32±0.35

Table C.2 The composition of Nd₂Fe₁₄B phase (Gray phase) in Nd_{2.7}Fe₁₄B_{1.4} layer of the Nd_{2.7}Fe₁₄B_{1.4}/Dy₂Fe₁₄B plus 2at% B/Nd_{2.7}Fe₁₄B_{1.4} pellet

Distance from the interface	Gray phase		
	Fe K-family	Nd L-family	Dy M-family
50 micron	69.18±0.36	27.79±0.32	3.03±0.43
	69.45±0.34	23.92±0.28	6.63±0.33
	71.19±0.35	24.28±0.29	4.53±0.26
	72.65±0.35	24.86±0.29	2.49±0.26
Average	70.62±0.35	25.21±0.30	4.17±0.32
100 micron	72.78±0.35	25.03±0.29	2.19±0.26
	72.65±0.35	22.22±0.26	5.13±0.24
	71.15±0.36	21.14±0.27	7.71±0.32
	71.38±0.35	21.77±0.26	6.85±0.31
Average	71.99±0.35	22.54±0.27	5.47±0.28
350 micron	70.80±0.35	24.88±0.29	4.31±0.26
	61.03±0.33	34.91±0.37	4.06±0.32
	67.21±0.35	28.95±0.33	3.88±0.27
	72.37±0.35	25.25±0.29	2.38±0.24
Average	67.85±0.345	28.50±0.32	3.66±0.27
600 micron	72.22±0.35	25.03±0.29	2.75±0.27
	71.81±0.35	24.90±0.29	3.28±0.26
	70.35±0.35	28.49±0.32	1.16±0.24
	71.46±0.35	26.14±0.3	2.40±0.26
850 micron	70.51±0.34	26.40±0.29	3.09±0.24
	71.96±0.34	25.02±0.28	3.02±0.25
	68.00±0.34	28.23±0.31	3.77±0.27
	71.86 ±0.34	25.54±0.28	0.26±0.23
Average	70.58±0.34	26.30±0.29	2.54±0.25
1000 micron	72.08±0.36	25.03±0.29	2.89±0.25
	72.38±0.36	26.64±0.31	0.98±0.42
	69.62±0.35	28.67±0.32	1.71±0.30
Average	71.36±0.36	26.78±0.31	1.86±0.32

Appendix D: This letter is for Figure 1.1 and 3.4



COPYRIGHT PERMISSION REQUEST

Please complete all contact information:

Name: Parawee Pumwongpitak

Title:

Company/Organization: Michigan Technological University

Address: 3761 Watkins Drive, Apt. L., Riverside, California, 92507

Phone: 906-370-1944

Email: ppumwong@mtu.edu

I am preparing an article/chapter for publication in the following formats (check as applicable):

Print Only ☐

Internet Only ☐

Print and Electronic Media ☒

The information will be used for (check as applicable):

Journal article ☐

Conference presentation ☐

Internal company records ☐

Dissertation ☒

Student course material ☐

Commercial publication* ☐

Please complete the following:

The article/chapter title will be: Chapter 3. Results and discussions

The publication title will be: Dysprosium Transport in Nd-Fe-B pellets

Publisher: Michigan Technological University, ProQuest

Planned date of publication: April 19, 2013

I hereby request permission for non-exclusive world rights for the above publication and all subsequent editions, revisions, and derivative works in English and foreign translations, in the formats indicated above from the following copyrighted content by **ASM International**:

Book ISBN:

Copyright date: The Alloy Phase Diagrams center : 2006-2013

Book/Publication title: Alloy Phase Diagram Database™

Author name(s): Tsai D.S., Chin T.S., Hsu S.E., Hung M.P.

Article title: B-Fe-Nd Phase Diagram

Text page numbers:

Figure numbers (with page numbers): Diagram number: 978565

Table numbers (with page numbers):

Signature

P. E.

Date 4/4/13

FOR ASM INTERNATIONAL USE ONLY:

I (we) grant permission requested above. Please ensure that ASM International receives proper credit as publisher by citing the above ASM publication as a reference and including the following: Reprinted with permission of ASM International. All rights reserved. www.asminternational.org

Sue Sellers

ASM International is a registered trademark of ASM International, Inc. All rights reserved. ASM International, Inc. is a registered trademark of ASM International, Inc. All rights reserved.

ASM International

4-5-2013

Date

*For Commercial Publications, a copyright permission fee of \$50 per figure will be assessed.

Exceptions can be made for reuse of content by its original authors.

ASM International, Permissions, 9639 Kinsman Road, Materials Park, Ohio 44073-0002
permissions@asminternational.org, 440-338-5151 x5465

Submit

Appendix E: This letter is for Figure 3.2



COPYRIGHT PERMISSION REQUEST

Please complete all contact information:

Name: Parawee Pumwongpitak

Title:

Company/Organization: Michigan Technological University

Address: 3761 Watkins Drive, Apt. L., Riverside, California, 92507

Phone: 906-370-1944

Email: ppumwong@mtu.edu

I am preparing an article/chapter for publication in the following formats (*check as applicable*):

Print Only ☐

Internet Only ☐

Print and Electronic Media ☒

The information will be used for (*check as applicable*):

Journal article ☐

Conference presentation ☐

Internal company records ☐

Dissertation ☒

Student course material ☐

Commercial publication* ☐

Please complete the following:

The article/chapter title will be: Chapter 3. Results and discussions

The publication title will be: Dysprosium Transport in Nd-Fe-B pellets

Publisher: Michigan Technological University, ProQuest

Planned date of publication: April 19, 2013

I hereby request permission for non-exclusive world rights for the above publication and all subsequent editions, revisions, and derivative works in English and foreign translations, in the formats indicated above from the following copyrighted content by **ASM International**:

Book ISBN: Copyright date: The Alloy Phase Diagrams center : 2006-2013

Book/Publication title: Alloy Phase Diagram Database™

Author name(s): Okamoto H.

Article title: Dy-Fe (Dysprosium-Iron) Phase Diagram

Text page numbers:

Figure numbers (with page numbers): Diagram number: 981146

Table numbers (with page numbers):

Signature *Pa. Ek* Date 4/4/13

FOR ASM INTERNATIONAL USE ONLY:

I (we) grant permission requested above. Please ensure that ASM International receives proper credit as publisher by citing the above ASM publication as a reference and including the following: Reprinted with permission of ASM International. All rights reserved. www.asminternational.org

Sue Sellers

ASM International

***For Commercial Publications, a copyright permission fee of \$50 per figure will be assessed.**

Exceptions can be made for reuse of content by its original authors.

4-5-2013

Date

ASM International, Permissions, 9639 Kinsman Road, Materials Park, Ohio 44073-0002
permissions@asminternational.org, 440-338-5151 x5465

Submit

Appendix F: This letter is for Figure 3.3



COPYRIGHT PERMISSION REQUEST

Please complete all contact information:

Name: Parawee Pumwongpitak

Title:

Company/Organization: Michigan Technological University

Address: 3761 Watkins Drive, Apt. L., Riverside, California, 92507

Phone: 906-370-1944

Email: ppumwong@mtu.edu

I am preparing an article/chapter for publication in the following formats (*check as applicable*):

Print Only ☐

Internet Only ☐

Print and Electronic Media ☒

The information will be used for (*check as applicable*):

Journal article ☐

Conference presentation ☐

Internal company records ☐

Dissertation ☒

Student course material ☐

Commercial publication* ☐

Please complete the following:

The article/chapter title will be: Chapter 3. Results and discussions

The publication title will be: Dysprosium Transport in Nd-Fe-B pellets

Publisher: Michigan Technological University, ProQuest

Planned date of publication: April 19, 2013

I hereby request permission for non-exclusive world rights for the above publication and all subsequent editions, revisions, and derivative works in English and foreign translations, in the formats indicated above from the following copyrighted content by **ASM International**:

Book ISBN: Copyright date: The Alloy Phase Diagrams center : 2006-2013

Book/Publication title: Alloy Phase Diagram Database™

Author name(s): Grieb B., Henig E.T., Schneider G., Petzow G.

Article title: B-Dy-Fe Phase Diagram

Text page numbers:

Figure numbers (with page numbers): Diagram number: 977949

Table numbers (with page numbers):

Signature *Pa. Ek* Date 4/4/13

FOR ASM INTERNATIONAL USE ONLY:

I (we) grant permission requested above. Please ensure that ASM International receives proper credit as publisher by citing the above ASM publication as a reference and including the following: Reprinted with permission of ASM International. All rights reserved. www.asminternational.org

Sue Sellers

ASM International

*For Commercial Publications, a copyright permission fee of \$50 per figure will be assessed.

Exceptions can be made for reuse of content by its original authors.

4-5-2013

Date

ASM International, Permissions, 9639 Kinsman Road, Materials Park, Ohio 44073-0002
permissions@asminternational.org, 440-338-5151 x5465

Submit